LATVIAN JOURNAL of PHYSICS and TECHNICAL SCIENCES

ISSN 0868 - 8257

(Vol. 56)

2019

SATURS

CONTENTS

СОДЕРЖАНИЕ

LATVIAN JOURNAL of PHYSICS and TECHNICAL SCIENCES

LATVIJAS FIZIKAS un TEHNISKO ZINĀTŅU ŽURNĀLS

ЛАТВИЙСКИЙ ФИЗИКО-ТЕХНИЧЕСКИЙ ЖУРНАЛ

Published six times a year since February 1964
Iznāk sešas reizes gadā kopš 1964. gada februāra
Выходит шесть раз в год с февраля 1964 года

2 (Vol. 56) • 2019

RĪGA

REDAKCIJAS KOLĒĢIJA

N. Zeltiņš (galvenais redaktors), A. Šternbergs (galvenā redaktora vietnieks), A. Ozols, A. Mutule, J. Kalnačs, A. Siliņš, G. Klāvs, A. Šarakovskis, M. Rutkis, A. Kuzmins, Ē. Birks, S. Ezerniece (atbild. sekretāre)

KONSULTATĪVĀ PADOME

J. Vilemas (Lietuva), K. Švarcs (Vācija), J. Kapala (Polija), J. Melngailis (ASV), T. Jëskelainens (Somija), J. Savickis (Latvija), Ā. Žīgurs (Latvija)

EDITORIAL BOARD

N. Zeltins (Editor-in-Chief), A. Sternberg (Deputy Editor-in-Chief), A. Ozols, A. Mutule, J. Kalnacs, A. Silins, G. Klavs, A. Sarakovskis, M. Rutkis, A. Kuzmins, E. Birks, S. Ezerniece (Managing Editor)

ADVISORY BOARD

J. Vilemas (Lithuania), K. Schwartz (Germany), J. Kapala (Poland), J. Melngailis (USA), T. Jeskelainens (Sweden), J. Savickis (Latvia), A. Zigurs (Latvia)

Korektore: O. Ivanova
Maketētājs: I. Begičevs

INDEKSĒTS (PUBLICĒTS) | INDEXED (PUBLISHED) IN

www.scopus.com
www.sciendo.com
EBSCO (Academic Search Complete, www.epnet.com), INSPEC (www.iee.org.com).
VINITI (www.viniti.ru), Begell House Inc/ (EDC, www.edata-center.com).

Izdevēji: Fizikālās enerģētikas institūts, LU Cietvielu fizikas institūts
Reģistrācijas apliecība Nr. 000700221
Redakcija: Krīvu iela 11, Rīga, LV-1006
Tel. 67551732
e-pasts: ezerniec@edi.lv
Interneta adrese: www.fei-web.lv

sciendo

LATVIAN JOURNAL OF PHYSICS
AND TECHNICAL SCIENCES
2019, N 2

DOI: 10.2478/lpts-2019-0008

PHYSICAL AND TECHNICAL ENERGY PROBLEMS

SYNTHESIS OF ELECTRONICALLY COMMUTATED SYNCHRONOUS MOTORS WITH PREDEFINED CHARACTERISTICS

L. Lavrinovicha, J. Dirba, K. Sejejs, E. Kamolins
Riga Technical University,
12/1 Azenes Str., Riga, LV-1048, LATVIA
e-mail: ludmila.lavrinovica@rtu.lv

The authors present a methodology for the calculation and optimisation of regulation laws that apply to electronically commutated synchronous motors with predefined characteristics. It is shown that the synchronous electronically commutated motors can provide predefined characteristics with the maintenance of high energy performance by simultaneously regulating supply voltage, excitation current and load angle.

Keywords: *electronically commutated motor, mechanical characteristic, synchronous motor*

1. INTRODUCTION

Development of semiconductors, microprocessors and motor production technologies makes it possible to solve issues of electric motors with predefined characteristics. The topicality of this task is based on a great variety of electrically driven equipment and the necessity to save energy. The best way to achieve this task is to use electronically commutated motors, which are based on synchronous motors operating in special modes together with a semiconducting commutator and feedback of the motor rotation speed. These types of electrical machines are known as having sufficient power density and efficiency to meet the criteria and requirements of modern electrical drives [1]–[3].

The analysis shows that depending on the commutator circuit and the type of motor excitation electronically commutated synchronous motors can provide a wide spectrum of motor characteristics that are similar to brushed DC motors with shunt, series or compound excitation [3], [4]. The paper [3] shows that in order to ensure the high efficiency of electronically commutated synchronous motors operating with variable load, it is necessary to regulate supply voltage U_1, excitation current I_2 and load angle θ.

Results of the studies, which have been carried out until nowadays, and

the modern microprocessor technologies allow us to formulate the task of motor synthesis and optimisation by combining these two stages in one.

2. METHODOLOGY FOR THE SYNTHESIS OF THE ELECTRONICALLY COMMUTATED SYNCHRONOUS MOTOR

The motor synthesis and optimisation task can be conditionally divided into several stages:

- development of the computer program for calculations and optimisation of motor characteristics;
- regulation rule calculations for supply voltage U_1, excitation current I_2 and load angle θ, which provide motor predefined characteristics in certain ranges of the variable load;
- electric motor optimisation in order to increase its efficiency during operation in special operation modes;
- determination of the spectrum for characteristics that can be useful to implement in the dimensions of one motor;
- practical implementation of supply voltage U_1, excitation current I_2 and load angle θ regulation.

Armature current I_1, electromagnetic torque M, electric power P_1, phase shift φ (angle between armature current and supply voltage) and magnetization current $I\mu$ of salient pole synchronous motors can be determined from relevant equations [5]:

$$I_1 = \frac{\sqrt{[U_1\ (\sigma\omega L_{ad}\sin\theta + r_1\cos\theta) - I_2\omega L_{ad} r_1]^2 + \rightarrow}}{r_1^2 + \sigma\omega^2 L_{ad}{}^2 A} \rightarrow$$
$$\rightarrow \frac{\rightarrow + \left\{ U_1\ \left[\omega L_{ad} A\cdot\cos\theta - r_1\sin\theta\right] - I_2\omega^2 L_{ad}{}^2\ A \right\}^2}{}; \quad (1)$$

$$M = \frac{mpL_{ad}\,[U_1(\sigma\omega L_{ad}\sin\theta + r_1\cos\theta) - I_2\omega L_{ad} r_1]}{r_1{}^2 + \sigma\omega^2\ L_{ad}{}^2 A} \times$$
$$\times\left(I_2 + \frac{[U_1\ (\omega L_{ad}\ A\cos\theta - r_1\sin\theta) - I_2\omega^2 L_{ad}{}^2\ A] \times B}{r_1{}^2 + \sigma\omega^2 L_{ad}{}^2\ A} \right); \quad (2)$$

$$P_1 = mU_1\left[\frac{U_1 r_1 + \frac{1}{2}U_1\omega L_{ad} A\sin 2\theta}{r_1{}^2 + \sigma\omega^2 L_{ad}{}^2\ A} + \frac{I_2\omega L_{ad}\left[\omega L_{ad} A\sin\theta - r_1\cos\theta\right]}{r_1{}^2 + \sigma\omega^2 L_{ad}{}^2\ A} \right]; \quad (3)$$

$$\mathrm{tg}\varphi = \frac{\omega L_{ad} \cdot \left\{ U_1 \cdot \left[\sigma \sin^2 \theta + A \cdot \cos^2 \theta \right] - I_2 \cdot \left[r_1 \sin\theta + \omega L_{ad} \cdot A \cos\theta \right] \right\}}{U_1 r_1 + 0.5 U_1 \omega L_{ad} \cdot A \cdot \sin 2\theta + I_2 \omega L_{ad} \cdot \left[\omega L_{ad} \cdot A \cdot \sin\theta - r_1 \cos\theta \right]} \quad (4)$$

$$I_\mu = \sqrt{I_1^2 + I_2^2 + 2 I_1 I_2 \sin(\varphi - \theta)} \quad (5)$$

where $A = \left(\frac{k_q}{k_d} + \acute{o} - 1 \right)$,

$B = \left(1 - \frac{k_q}{k_d} \right)$;

ω is the angular frequency of armature current;

p is the number of pole pairs;

m is the number of phases;

L_{ad} is the inductance corresponding to the flux of armature reaction;

σ is the leakage factor of the armature winding;

r_1 is the active resistance of the armature winding;

k_d, k_q is the field shape factors.

Equations (1)–(5) correspond to the general case – the salient pole synchronous machine with an excitation winding. In case if k_q/k_d =1 or I_2 = 0 it is possible to obtain equations for non-salient pole synchronous machine or synchronous reluctance machine, respectively. In these cases, equations are more simplified. Given the fact that most applied motors in modern electric drives are motors with permanent magnets, which have no excitation winding, permanent magnets have to be conditionally replaced by equivalent winding current I_2.

Motor mechanical power P_2 can be calculated by losses of armature current deduction from electric power P_1. The losses of armature current are proportional to I_1^2, excitation winding losses (proportional to I_2^2, mechanical losses (proportional to ω^3) and the losses in the motor core proportional to $\omega^{1.3}$). The efficiency factor of the machine is determined as $\eta = P_2/P_1$. Starting torque M_p is determined by equation (2) when $\omega = 0$:

$$M_p = \frac{mpL_{ad}U_1}{r_1} \cdot [I_2 \cos\theta - \frac{U_1}{2r_1} \cdot B \sin(2\theta)]. \quad (6)$$

In deriving of equations (1)–(5), it is assumed that the phase currents and voltages are sinusoidal, the excitation current has been transmitted to the armature winding, but the magnetic circuit of the motor is unsaturated.

The computer program for calculations and optimisation of motor characteristics is convenient to be implemented in MS EXCEL with the possibility to print out all necessary graphs and tables.

In case of a synchronous motor without regulation, when U_1 = const, I_2 = const and θ = const, calculations of the motor characteristics are relatively simple. Motor parameters I_1, M, P_1, $I\mu$, cosφ, P_2 and η, which are used for the definition of the motor characteristics, are calculated from basic equations (1)–(5) of synchronous machines, taking angular frequency ω as a variable value.

If regulation of the motor parameters is provided, the synthesis and optimisation of the regulation laws for a motor with predefined characteristics are useful to be executed simultaneously.

For the optimisation of synchronous motor characteristics, the following methodology can be suggested.

First, the desirable characteristics, for example, mechanical characteristic ω = $f(M)$ is pre-set by the graph or table data. Then the permitted ranges of variable parameters I_2, θ and U_1 are determined. Further calculations are done in the following order: for every point of the predefined characteristic ω = $f(M)$ values of I_2, θ and U_1 are calculated by the use of equations (1)–(5) that provide, first, the predefined values of ω and M, and second, optimisation criteria – minimum losses in the studied motor (or maximum η). Regulation rules as $I_2 = f(M)$, θ = $f(M)$ and $U_1 = f$(M) can be obtained by repeating the same calculations for over several points (usually 5–10) of predefined characteristic ω = $f(M)$. Depending on the practical implementation in a particular case, regulation rules for the studied motor can easily be obtained as functions of anchor current I_1 or over motor parameters.

There are two methodologies used for motor optimisation.

In the first case, the optimisation is carried out by calculation of all possible combinations of I_2, θ and U_1. For this purpose, before starting the calculation, it is necessary to determine both the range and the step of variation for each of the variable parameters. In addition, it is necessary to specify the required values of the torque M and the angular frequency ω at several points (5–10 points) of the predefined characteristic. The allowable error of the solution has to be specified as well.

Since values of all variables I_2, θ and U_1 should be changing during the searching of a solution, three nested loops are formed in the program. The values of voltage U_1 are changing in the outer loop, the load angle θ – in the middle loop, and the excitation current I_2 – in the inner loop. The corresponding values of torque are determined for each resulting combination of parameters I_2, θ and U_1. The purpose of this search is to find such values of the variable parameter for which, with a given accuracy, the value of M_i is in the vicinity of the desired value M. If the solution is located between present and previous values of the searched M, more detailed search is performed by dividing the segment in half. However, any solution, which is found in this way, is only one of several possible options. Combinations of variable parameters I_2, θ, U_1 with over parameters in interest that ensure maximum efficiency η_{max} are saved.

Such search is repeated for each point of the predefined characteristic ω = $f(M)$.

Characteristic $\eta = f(M)$ and regulation laws $I_2 = f(M)$, $\theta = f(M)$, $U_1 = f(M)$ that are based on founded combinations of variable parameters are plotted at the beginning of the program.

In the second optimisation case, the calculations are repeated for different initial points that are uniformly distributed in the region of permissible values of variable factors [5], [6]. If the optimisation invariably ends with practically the same values of I_2, θ, U_1, this indicates that the obtained solution is a global, rather than a local maximum.

Analysis of both optimisation methodologies shows that values of η_{max} obtained by two methods do not differ by more than 5 %.

It is necessary to point out that during the calculation and optimisation process for providing the predefined characteristic, all variables I_2, θ and U_1 cannot be considered as independent variables, but only any two of them. Therefore, each time when values of two variables are chosen at random, for example, I_2 and θ, the value of the voltage U_1 correspondently is calculated from equations (1)–(5).

3. CALCULATIONS OF REGULATION LAWS FOR ELECTRONICALLY COMMUTATED SYNCHRONOUS MOTORS

Below, as an example, the proposed methodology is illustrated by non-salient pole and salient pole three-phase synchronous motors.

Parameters for studied non-salient pole synchronous motor are as follows: $r_1 = 2{,}5\ \Omega$, $\sigma = 1{,}07$, $L_{ad} = 0{,}3$ H, $p = 3$. Figure 1 shows two predefined mechanical characteristics No. 1 and No. 2 for the studied motor.

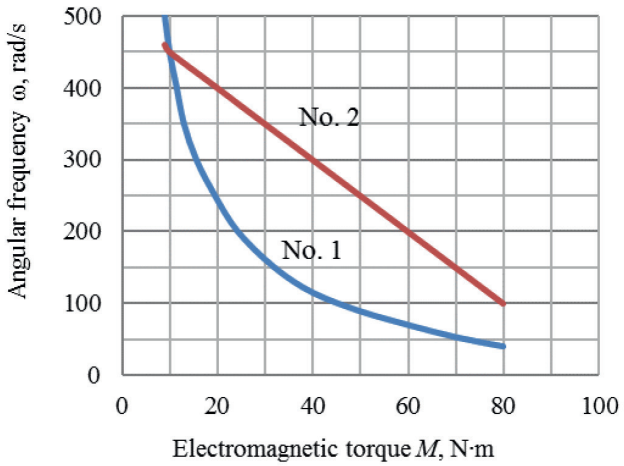

Fig. 1. Predefined mechanical characteristics in the first example.

Regulation laws $I_2 = f(M)$, $\theta = f(M)$, $U_1 = f(M)$ and $\eta = f(M)$ for studied non-salient poles that provide predefined mechanical characteristics (Fig. 1) are shown in Fig. 2. In this case, the minimum losses in the studied motor (or maximum efficiency) are accepted as optimisation criteria. The restriction for supply voltage U_1 is accepted, which does not allow increasing it above the nominal value.

a)

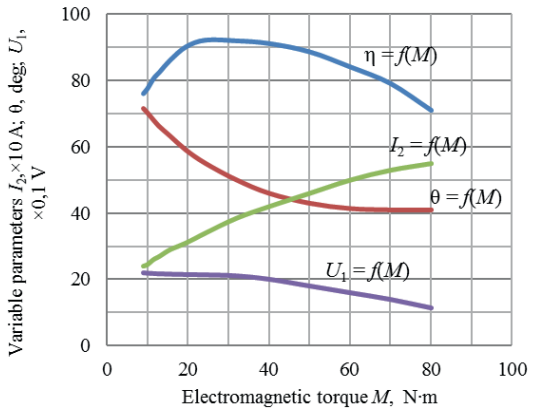

b)

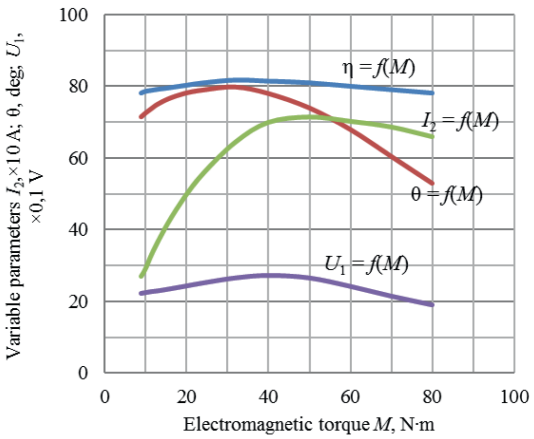

Fig. 2. Regulation laws $I_2 = f(M)$, $\theta = f(M)$, $U_1 = f(M)$ and $\eta = f(M)$ for defining non-salient motor characteristics No. 1. (a) and No. 2. (b).

Figures 1 and 2 show that simultaneous regulation of the motor parameters I_2, θ and U_1 can provide the motor predefined characteristics with high efficiency.

Parameters of the studied salient pole synchronous motor: $r_1 = 2.5$ Ω, $\sigma = 1.07$, $L_{ad} = 0.3$ H, $p = 3$ and $k_q/k_d = 0.8$. Predefined mechanical characteristics No. 1 and No. 2 for the second example are presented in Fig. 3.

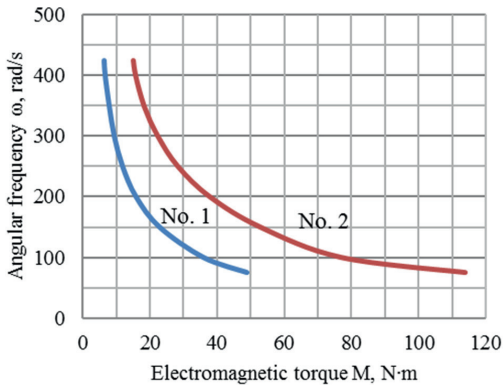

Fig. 3. Predefined mechanical characteristics for the second example.

Regulation laws $I_2 = f(M)$, $\theta = f(M)$, $U_1 = f(M)$ and $\eta = f(M)$ for studied salient poles motor that provide predefined mechanical characteristics (Fig. 3) are shown in Fig. 4.

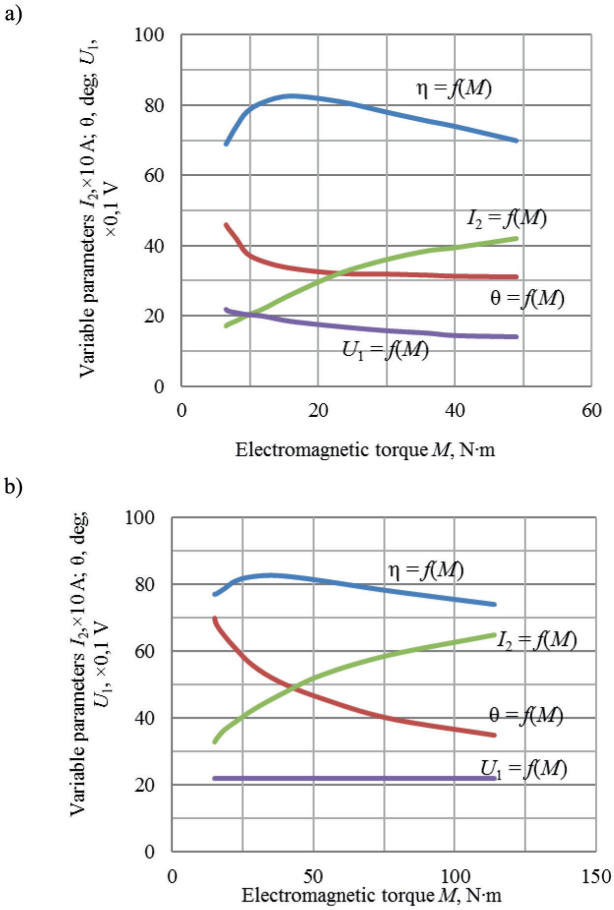

Fig. 4. Regulation laws U_1, I_2, $\theta = f(M)$ and $\eta = f(M)$ for defining salient pole motor characteristics No. 1. (a) and No. 2. (b).

Comparison of calculated characteristics with the results obtained in the experiments shows that the proposed methodology makes it possible to obtain results, which reflect the nature of the physical process in the motor with a sufficient degree of accuracy.

The analysis shows that by reducing the number of parameters under regulation up to two or just one, the predefined mechanical characteristics can be provided in a narrower range versus to the case where all three parameters are under regulation.

4. THE PROPOSED SYNCHRONOUS MOTOR CONTROL SYSTEM

Functional scheme of the synchronous motor control system for validation of the proposed methodology is shown in Fig. 5.

To increase the reliability and efficiency of the variable speed drive of the synchronous motor, a sensorless control circuit has been implemented. The drive

control method is speed-independent and it is based on commutation thresholds by sensing the terminal voltage differences between two control states of each phase of the armature winding. From these differences, the actual rotor position θ can be calculated using rotor speed and position calculation algorithm [7], [8].

For the terminal voltage and current measurement, a block with voltage and current sensors for each phase of the armature winding is used. This control method is effective from the start-up of the synchronous motor up to 100 % PWM duty cycle of the three-phase inverter. When the PWM duty cycle approaches 100 %, the rotor position is obtained by calculation of the zero-crossing point (ZCP) of back-electromotive force (back-EMF), thus achieving full-speed range sensorless control of the synchronous motor [9].

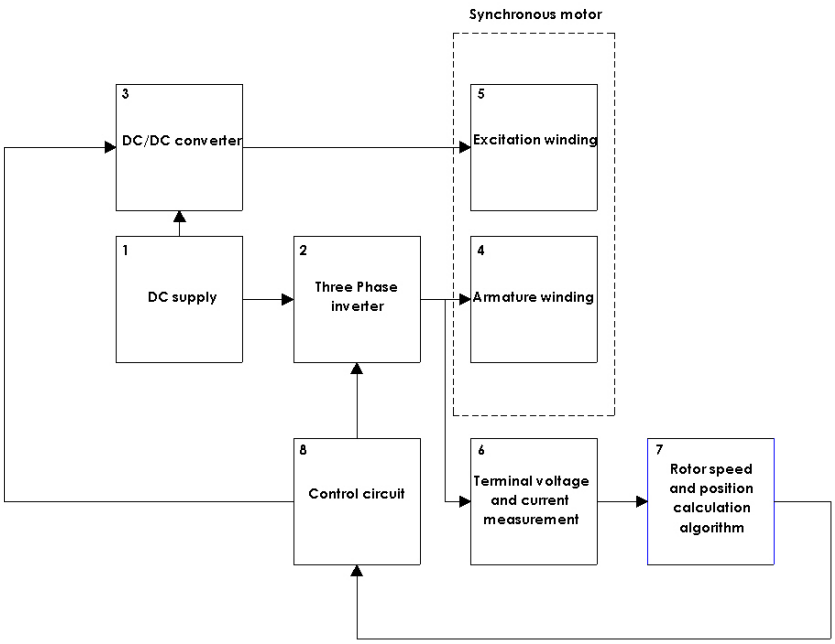

Fig. 5. Functional scheme of the synchronous motor control system.

5, CONCLUSIONS

Based on the results obtained within the framework of the conducted research, the following conclusions can be drawn:

1. The proposed methodology makes it possible to synthesize motors with predefined and variable characteristics.
2. Reducing the number of parameters under regulation narrows the ranges of the set characteristics.
3. In the proposed synchronous motor control system position closed-loop control is used at the beginning of the motor operation.
4. Commutation instants are acquired directly instead of a phase shift from the zero-crossing point (without low-pass filters) in the commutation threshold-based method. Therefore, there are no phase delay problems.

5. Precise parameters of the synchronous motor are not needed.
6. The proposed control system is easy to implement because it requires no extra hardware components (low cost) and there are no complicated computations.

REFERENCES

1. Irimia, N. D., & Lazar, F.I. (2017). A comparative study of different BLDC motor construction types used in automotive industry under specific command strategies. In *22nd IMEKO TC4 International Symposium & 20th International Workshop on ADC Modelling and Testing*, 14–15 September, 2017, Romania.
2. Olusegun, S. (2007). Model reference adaptive control of a permanent magnet brushless DC motor for UAV electric propulsion system. In *33rd Annual Conference of the IEEE Industrial Electronics Society*, 5–8 November 2007, Taipei, Taiwan.
3. Dirba, J., Lavrinovicha, L., Levins, N., & Pugachevs, V. (2012). Application of synchronous brushless motors in electric hand tools. *Latvian Journal of Physics and Technical Sciences*, *49*(1), 29–34. ISSN 0868-8257.
4. Lavrinovicha, L., & Dirba, J. (2015). *Brushless synchronous motors with external rotor*. Riga: RTU Publishing House. (in Latvian)
5. Auzins, J., & Janusevskis, A. (2011). *Planning and analysis of experiments*. Riga: RTU Publishing House. (in Latvian)
6. Eglajs, V. (1980). *Algorithm for intuitive search to optimize complex systems. Problems of dynamics and strengths*. Riga: Zinatne Publishing House, pp. 28–33. (in Russian)
7. Lin, N., Qiu, J., & Shi, C. (2018). A Full-speed range sensorless control scheme of brushless DC motor based on saliency effects. In *21st International Conference on Electrical Machines and Systems (ICEMS)* (pp. 1654–1658), 7–10 October 2018, Korea.
8. Miller, T.J.E. (2001). *Electronic control of switched reluctance machines*. Newnes Power Engineering Series.
9. Ahmad, F., Zaid, M., & Pandey, M. (2018). Sensorless control of brushless DC motor by zero-crossing detection pulse generation with adaptive power factor control technique. In *IEEE International Conference on Environment and Electrical Engineering and IEE Industrial and Commercial Power Systems Europe (EEEIC / I&CPS Europe)*, 12–15 June 2018, Palermo, Italy.

SINHRONO VENTIĻDZINĒJU SINTĒZE AR IEPRIEKŠ UZDOTĀM RAKSTURLĪKNEM

L. Lavrinoviča, J. Dirba, K. Sējējs, E. Kamoliņš

K o p s a v i l k u m s

Piedāvāta regulēšanas likumu aprēķinu un optimizācijas metodika ventiļdzinējiem ar iepriekš uzdotām raksturlīknēm. Parādīts, ka vienlaikus regulējot barošanas spriegumu, ierosmes strāvu un slodzes leņķi, sinhronais ventiļdzinējs var nodrošināt iepriekš uzdotās raksturlīknes, saglabājot augstus enerģētiskos rādītājus.

05.03.2019.

sciendo

LATVIAN JOURNAL OF PHYSICS
AND TECHNICAL SCIENCES
2019, N 2

DOI: 10.2478/lpts-2019-0009

FORMATION AND STUDY OF STATIC AND DYNAMIC CHARACTERISTICS OF ELECTRONICALLY CONTROLLED DIESEL ENGINE

P. Dumenko[1], S. Kravchenko[2], A.Prokhorenko[2], D. Talanin[2]
[1]DiGas Ltd.
31 Talsu soseja, K-17-34, Jurmala, LV-2016, LATVIA
e-mail: p.dumenko@digasgroup.lv
[2]National Technical University "Kharkiv Polytechnic Institute"
2 Kyrpychova Str., Kharkiv, 61002, UKRAINE

Manufacturing companies of electronic control systems of diesel engines protect access to a program operation algorithm of the regulator that makes impossible adjustments and settings of its work, for example, at re-equipment or operational development of a new diesel engine. Therefore, it is important to acknowledge the solution of the scientific and technical problem of an effective and reliable system creation of electronic control of diesel fuel supply with an open program algorithm of its work. During the current research, settlement and experimental studies of a diesel engine supplied with a system of electronic control of a crankshaft rotation frequency developed by the authors show rather high adequacy in results. The dynamic mathematical model of the single-cylinder diesel engine supplied with the electronic regulator of rotation frequency has been developed and verified.

Keywords: *diesel engine, electronic regulator, mathematical modelling*

1. INTRODUCTION

At the moment, leading countries continue to improve motor vehicles in order to achieve new qualities for consumers, e.g., improved controllability, ergonomics, fuel efficiency, reduction of harmful emissions into the atmosphere, improvement safety, comfort, noise level, vibration, etc. This primarily concerns the improvement of the internal combustion engine (ICE), especially diesel engines.

It is known that the diesel engine works in the wide range of the load, high-speed and thermal modes. At the same time, reduction of harmful emissions, fuel consumption, noise and vibration of the engine are promoted by such organization of management process of this object, which provides the most high-quality transitional processes in all fields of its possible operating modes. It is indisputable that this optimization is impossible without implementation of special algorithms by electronic control systems.

However, the cost of electronic systems of regulation remains rather high, and their service and repair demand existence of expensive and difficult equipment, as well as highly skilled personnel. Besides, manufacturing companies of such systems protect access to a program operation algorithm of regulator that makes impossible adjustments and settings of its work, for example, at re-equipment or operational development of a new diesel engine.

The scientific publications devoted to development and research of algorithms of electronic control systems of engines practically are absent, and those which are known differ in laconicism of material supply.

For example, in publications [1], [2] there is information about the practical creation of electronic control systems for diesel engines, where fuel supply is controlled not by the rail of fuel pump, but by the high-pressure bleed solenoid valve. These publications consider such themes as the design, schemes, results of experimental studies and mathematical modelling, but the description of the algorithms is not disclosed by the authors. In addition, the features of diesel locomotive operation do not allow transferring the control algorithm on engines for land transport or special equipment.

Recently there has been a set of scientific publications describing the research devoted to introduction of electronic control by the engine test bench [3], [4]. The aim of these studies is reproduction of engine transient test cycles of the engine for definition of their ecological indicators. However, here, though being novel, the problem of management is solved by absolutely other object – the loading device.

There are also publications on the development of control algorithms for individual systems of an internal combustion engine – a fuel pressure accumulator [5], an air supply system [6], an exhaust gas recirculation system [7], etc. that also do not relate directly to the regulation system of the engine high-speed mode.

The publication [8] is the most appropriate material on the formulation of the problem and the methods. Authors of the research have used a control algorithm based on the interpolation of the static characteristics of the regulator stored in the controller in tabular form. This approach has some disadvantages because such organisation of calculations introduces additional load on the central processor of the controller and leads to an increase in the intrinsic time (inertia) of the electronic regulator.

Therefore, it is important to acknowledge the solution of the scientific and technical problem on creation of an effective and reliable system of electronic control of diesel fuel supply with an open program algorithm of its work.

The aim of this article is to conduct experimental studies of a diesel engine supplied with a system of electronic control of rotation frequency of a crankshaft developed by the authors to confirm its reliable performance and efficiency.

2. THEORETICAL PART NO.1: BASICS OF THE ALGORITHMIZATION OF THE ELECTRONIC ALL-MODE DIESEL REGULATOR

For the synthesis of the electronic control algorithm for the rail of a high-pressure fuel pump (HPFP), a scientific approach has been applied based on the

analogy with the operation of an all-mode mechanical spring-lever speed controller of direct action. Mechanical all-mode regulators of diesel engines provide accepted (but, not always optimum) operational regulatory characteristics as well as are rather reliable units.

Let us consider operation of such a mechanical all-mode regulator with a variable tightening of a spring. Its schematic diagram is provided in Fig. 1. The structural logic diagram (Fig. 2) corresponds to this scheme, which is constructed on the basis of replacement of physical processes (linear movements of links or operating forces) with information ones. For example, movement of the coupling of a sensitive element under the influence of inertia force of the rotating mass of freights can be presented as a certain algorithm of measurement of rotation speed, and spring tightening force – as an algorithm of processing of change of the main external influence. From this point of view, the lever of the regulator can be presented as a certain calculator whose equilibrium position unambiguously defines value of an output signal of movement of a rail of HPFP, (*Hp*).

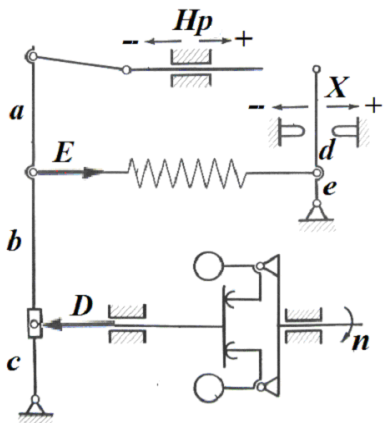

Fig. 1. The all-mode regulator with a variable tightening of a spring. Schematic diagram.

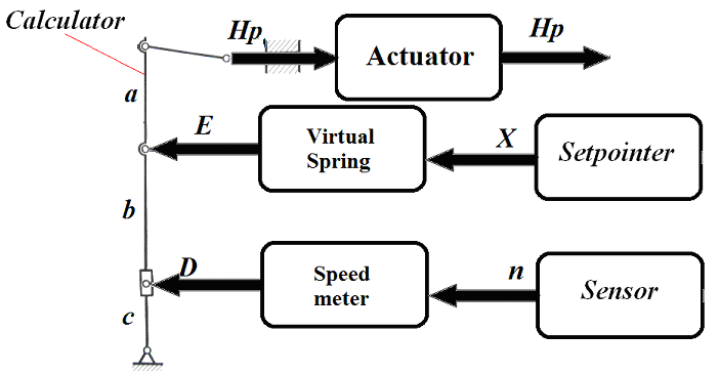

Fig. 2. Scheme of information analogy of operation of the all-mode regulator.

Then a condition of static balance of the all-mode regulator with a variable tightening of a spring is possible to describe by mathematical equality:

$$E \cdot \left(b + c\right) = D \cdot c \,. \tag{1}$$

Here E is a conditional restoring force, which is similar to regulator spring tightening force. This force consists of force of a preliminary tightening of a spring (E0) and its current deformations brought to the lever connected with the movement of a control lever (X) and a rail of HPFP (Hp):

$$E = E_0 + C \cdot \overline{X} \cdot \left(X_{\max} - X_{\min}\right)\frac{e}{d+e} - C \cdot \overline{Hp} \cdot \left(Hp_{\max} - Hp_{\min}\right)\frac{b+c}{a+b+c}, \tag{2}$$

where C – virtual coefficient of rigidity of a spring, N/m. *With line in this formula and further relative sizes are designated.*

The conditional supporting force $D = f\left(\omega\right)$ – in fact, is a measuring instrument of rotation speed. Let us assume that it complies with linear dependence. Then:

$$D = K \cdot \overline{\omega} \cdot \left(\omega_{\max} - \omega_{\min}\right) = K\frac{\pi}{30}\overline{n} \cdot \left(n_{\max} - n_{\min}\right) \cdot \tag{3}$$

In this formula, the constant coefficient of proportionality K conditionally has dimension of Ns (an analogue of inertial coefficient of the mechanical regulator).

After substitution of expressions (2) and (3) in the initial equation (1) and their simple transformation it is possible to come to the general equation:

$$\frac{E_0}{C\left(Hp_{\max} - Hp_{\min}\right)} \cdot \frac{a+b+c}{b+c} + \frac{X_{\max} - X_{\min}}{Hp_{\max} - Hp_{\min}} \cdot \frac{e\left(a+b+c\right)}{\left(d+e\right)\left(b+c\right)} \cdot \overline{X} - \overline{Hp} =$$

$$= \frac{\pi}{30} \cdot \frac{K\left(n_{\max} - n_{\min}\right)}{C\left(Hp_{\max} - Hp_{\min}\right)} \cdot \frac{c\left(a+b+c\right)}{\left(b+c\right)^2}\overline{n}.$$

It is visible that in this equation there are constants, which we will designate as follows:

$$A_1 = \frac{E_0}{C\left(Hp_{\max} - Hp_{\min}\right)} \cdot \frac{a+b+c}{b+c}, \quad A = \frac{X_{\max} - X_{\min}}{Hp_{\max} - Hp_{\min}} \cdot \frac{e\left(a+b+c\right)}{\left(d+e\right)\left(b+c\right)},$$

$$B = \frac{\pi}{30}\frac{K\left(n_{\max} - n_{\min}\right)}{C\left(Hp_{\max} - Hp_{\min}\right)} \cdot \frac{c\left(a+b+c\right)}{\left(b+c\right)^2}.$$

Then we have record of equation (1):

$$\overline{Hp} = A_1 + A \cdot \overline{X} - B \cdot \overline{n} \,. \tag{4}$$

The received equation (4) is a required algorithm of the electronic regulator operation. Using it is possible to calculate static characteristics of the regulator in the form of dependence $\overline{Hp} = f\left(\overline{X}, \overline{n}\right)$, and selection of values of coefficients of A_1, A

and B – set their required look. The following values of coefficients were accepted: $A_1 = 0.58$, $A = 1.22$ and $B = 1$.

3. EXPERIMENTAL PART NO. 1: IMPLEMENTATION OF A CONTROL SYSTEM AT THE RESEARCH MOTOR BENCH

To check the operability of the described operation algorithm of the electronic regulator of a crankshaft rotation frequency, engine testing studies were performed. The engine (the cylinder sizes: diameter of 120 mm, a piston stroke of 140 mm) was used, which was mounted on the laboratory test bench. This engine was the single-cylinder diesel with power up to 30 kW with a crankshaft rotation frequency from 700 to 1400 min^{-1}. Diesel engine test bench differed in the following design features:

- Injection of fuel in a cylinder was carried out by the high pressure fuel feeding system with the individual fuel pump (Unit Pump System).
- The engine lubrication system was autonomous.
- The cooling system – liquid, autonomous, with separate streams of cooling liquid in the block and a head of a cylinder.
- Engine start was carried out by means of the electric load device, which was part of the test bench.
- The engine had the mechanism of equilibration of inertia forces like *Lanchester*.
- In a head of a cylinder, the gas channel for installation of the indication sensor was implemented.

Besides, the test bench was equipped with all necessary devices and sensors for carrying out measurements of the current operation parameters of the engine.

The function chart of the developed electronic system of automatic control (SAC) of the diesel is shown in Fig. 3. As it is seen from the drawing, external and internal influences of such SAC are: $X(t)$ – the current position of governing body of the engine, $n(t)$ – the current rotation frequency of a crankshaft of the engine, Hp – position of governing body of fuel feeding (rail of HPFP), Bc – cyclic supply of fuel by HPFP and $Mc(t)$ – the loading resistance moment. *The letter* t *designates the current time.*

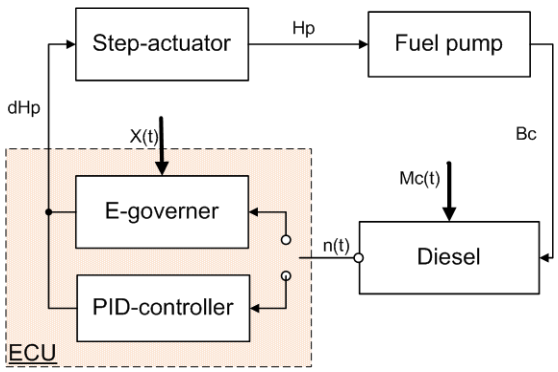

Fig. 3. Function chart of the electronic regulator of crankshaft rotation frequency.

The main components of the developed system of the electronic regulator are: ECU on *ATmega328* microcontroller; actuator; position sensors of a pedal of an accelerator, the «*Start*» and «*Auto*» buttons intended for initialization, according to the engine starting modes and PID regulation. Step actuator developed by company «*DigasGroup*» (Latvia) was used as the actuator for the drive of a rail of the fuel pump.

The accelerator pedal sensor was intended for registration of movement of a control lever and transmitted the corresponding signal to ECU.

Crankshaft rotation frequency was calculated by time of the period of signal of the inductive sensor installed opposite to a flywheel on which the magnetic plate was located.

The microcontroller processed primary received information from sensors, the "Start" and "Auto" buttons and implemented the program control algorithm put in it. By processing results of these signals, the microcontroller reacted via the actuator. Contact of the microcontroller with the actuator was implemented through the protocol of data transmission MAX-485.

ECU had the converter of interfaces USB-UART through which connection to the personal computer for its programming was carried out.

As the interface, 16 symbolical liquid crystal indicator was used on which the current information was transmitted: relative provision of a rail of the fuel pump and control lever, operating mode of the regulator, etc. Electronic regulator does not demand change of a design of the fuel pump; it is flexible and universal in regulation, can be installed on various types of diesel engines.

4. EXPERIMENTAL PART NO. 2: STATIC AND DYNAMIC CHARACTERISTICS OF THE DIESEL

The performed motor tests of a control system on the studied diesel showed that at introduction of electronic regulation on the equilibrium modes stability of crankshaft rotation frequency considerably increased (to $\Delta n = \pm 2$ min^{-1}) irrespective of fuel quality, technical condition of the engine, environmental conditions and other external factors.

The program of the performed tests in the form of a set of pairs of setting regime parameters was the following: "relative position of governing body of X – *Mc* loading resistance moment size" and the measured indicators corresponding to them: crankshaft rotation frequencies *n*, the current relative provision of a rail of HPFP *Hp* and mass hour fuel consumption.

The results received during tests allowed:

1. Experimentally confirming a type of static characteristic of the electronic regulator.
2. Defining and visualising regulatory characteristics of the diesel (provided in Fig. 4) – dependence of value of relative effective torque $\overline{Me}$ of the crankshaft rotation frequency *n* at various constant provisions of governing body of X.

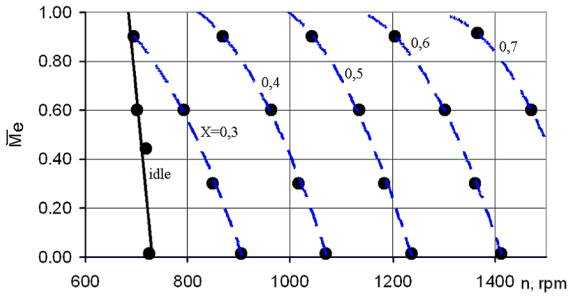

Fig. 4. Regulatory characteristics of the diesel engine.

3. Defining and visualising static characteristic of HPFP of the studied diesel engine (provided in Fig. 5) – dependence of relative value of its volume cyclic supply of fuel on the rotation frequency of crankshaft *n* at various constant provisions of governing body of X.

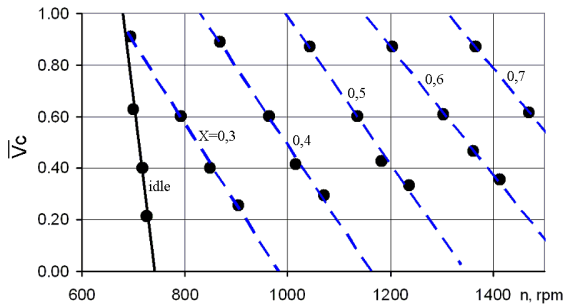

Fig. 5. Static characteristic of HPFP with the regulator.

4. Synthesising a basic matrix of fuel feeding of $Bc = f(n, X)$ for the current diesel necessary for creation of more complex system of management on the basis of predictive model (*Model Predictive Control*). This matrix was received by the method of interpolation-extrapolation of data in 22 separate experimental points. Graphically this matrix is presented in the surface form in Fig. 6. In the same place, values of the experimental data forming a basis for synthesis of the table are shown.

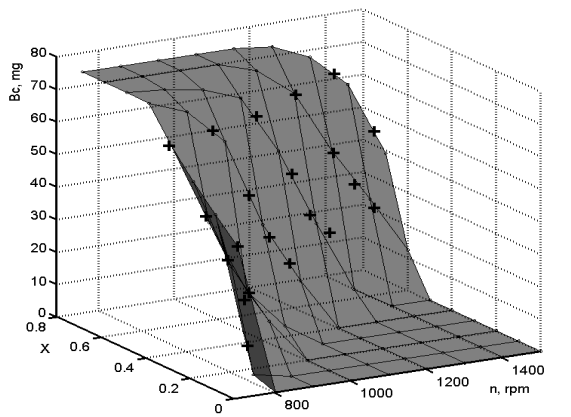

Fig. 6. The synthesized basic table of fuel feeding with experimental points (+).

Apparently from the provided drawings, the results received during the experiment did not contradict the standard requirements of regulation systems of diesel engines of different functions, especially in transport. Besides, the carried tests of the engine showed that the use of the offered electronic regulator allowed reducing time of transition processes between the required set modes.

For development and verification of a dynamic mathematical model of the studied diesel control system, records of a temporary track of the crankshaft current speed were received at the determined change of position of governing body of the engine. Example is given in Fig. 7.

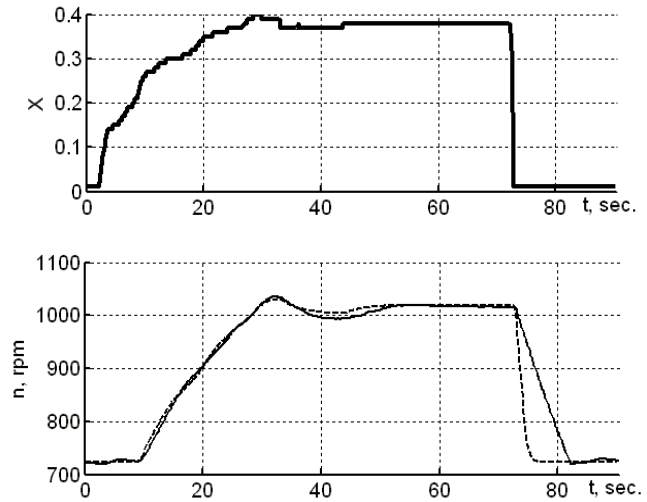

Fig. 7. Dynamic characteristics and results of mathematical modelling of an electronic system of regulation: ---- calculation; —— experiment.

5. THEORETICAL PART NO. 2: DESCRIPTION AND VERIFICATION OF MATHEMATICAL MODEL OF DYNAMICS OF A CONTROL SYSTEM

The calculation scheme of mathematical model of the developed electronic control system is provided in Fig. 8. In the form of internal information communication, the following sizes used as system coordinates are designated: ΔHp – the rejection of the provision of a rail of HPFP demanded for achievement of the equilibrium mode; $\Delta Hp'$ – the valid deviation of a rail of HPFP from equilibrium situation; $\Delta\omega$ – the current deviation from equilibrium value of angular speed of a crankshaft; ω_0 – a value of angular speed of the set equilibrium mode; n – an absolute value of rotation frequency of the engine; X – position of governing body of the engine.

For the description of the movement of a crankshaft of the engine, we use the known differential equation

$$J\frac{d\omega}{dt} = Me - Mc \cdot \tag{5}$$

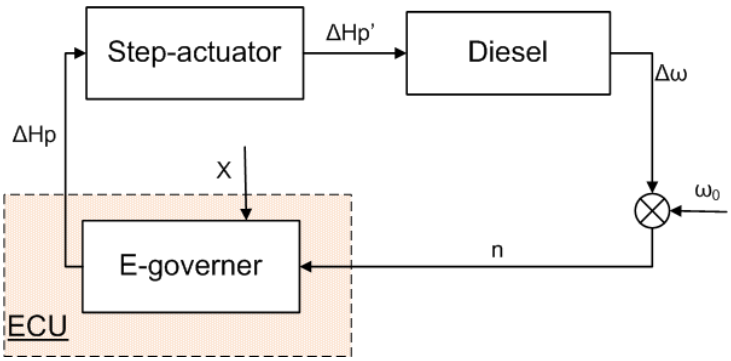

Fig. 8. Calculation scheme of mathematical model.

Assuming that the effective torque of the engine Me is linearly proportional to the size of cyclic supply of fuel Bc (that is fair for naturally aspirated engine), which unambiguously is determined by the current valid position of a rail of HPFP Hp'.

$$Me = f(Bc) = f(Hp') = A_A \cdot Hp'.$$

We also consider that the loading resistance moment M_C linearly depends on the angular crankshaft rotation speed.

$$Mc = f(\omega) = B_B \cdot \omega.$$

Here A_A, B_B – constant coefficients of proportionality.

Equation (5), taking into account a small deviation from the equilibrium mode Δ, is as follows:

$$J\frac{d(\omega_0 + \Delta\omega)}{dt} = A_A \cdot (Hp'_0 + \Delta Hp') - B_B \cdot (\omega_0 + \Delta\omega).$$

Considering a preliminary condition of the steady, equilibrium mode $Me(Hp'_0) = Mc(\omega_0)$, and zero derivative of constants, it could be simplified and given to the normalized look:

$$J\frac{d\Delta\omega}{dt} = A_A \cdot \Delta Hp' - B_B \cdot \Delta\omega. \quad (6)$$

The received equation (6) was the main settlement equation of mathematical model. Its numerical decision relatively $\Delta\omega$ allowed defining the current deviation of rotation frequency from its equilibrium value n_0:

$$\Delta n = 9.549 \cdot \Delta\omega.$$

Then the absolute value of the current frequency of rotation would be $n = n_0 + \Delta n$.

The required value of equilibrium provision of a rail of HPFP (mathematical description of work of an algorithm of ECU) for the current cycle was calculated by formula (4) taking into account that $Hp = Hp_0 + \Delta Hp$, where $\Delta Hp = A_1 + A \cdot X - B \cdot n - Hp_0$.

Writing up the differential equation of the movement of a rail of HPFP, it was accepted that it was without inertial part, but its movement was implemented to constant relative linear speed $C = \frac{d\Delta Hp'}{dt} = 0.0415$ s^{-1}. At the same time, its movement continuously continued before achievement of the set equilibrium situation $Hp = Hp_0 + \Delta Hp$ and takes time $\Delta t_K = \frac{\Delta Hp}{C}$. Therefore, change in the valid rejection of the position of a rail of HPFP in time could be described by the integrated equation $\Delta Hp' = C\int_{t_0}^{t_0+\frac{\Delta Hp}{C}} dt$.

The general algorithm of creation of calculations for the described mathematical model has the following sequence.

1. The current time interval for numerical integration on i-th step:
$$\Delta t_i = 120/n_{i-1}.$$
2. The current required rejection of the provision of a rail of HPFP for achievement of the equilibrium mode:
$$\Delta Hp_i = A_1 + A \cdot X_i - B \cdot n_{i-1} - Hp_0.$$
3. The current valid rejection of the provision of a rail of HPFP in each timepoint $t_i = t_{i-1} + \Delta t_i$ till moment $t_K = t_0 + \Delta t_K$:
$$\Delta Hp_i' = C\left(t_i - t_0\right).$$
4. Current deviation of crankshaft angular speed:
$$\Delta\omega_i = \frac{1}{J}\left(A_A \cdot \Delta Hp_i' - B_B \cdot \Delta\omega_{i-1}\right)\Delta t_i + \Delta\omega_{i-1}.$$
5. Current value of rotation frequency of the engine:
$$n_i = n_0 + \frac{30}{\pi}\Delta\omega_i.$$

After verification of the mathematical model consisting in selection of values of the mass moment of inertia of mobile parts of engine J and coefficients of proportionality A_A, B_B in equation (6), comparative calculation was carried out for the received experimentally temporary track of the current speed of a crankshaft $n(t)$ at the determined change of position of governing body of the engine $X(t)$. Its results are shown in the experimental graph (Fig. 7). At the same time, values J = 30 kg×m^2 were accepted (used single-cylinder engine had a massive flywheel), A_A = 1375 Nm, B_B = 0.05 Nm.

As it is seen from the drawing, the model rather adequately repeats an experimental track that validates the developed calculation procedure and allows using this mathematical model as a tool for carrying out further settlement studies.

6. CONCLUSIONS

As a result of the present research the following main results have been received:

1. Theoretical justification of synthesis of a program operation algorithm of the electronic regulator of diesel engine rotation frequency has been made.
2. The system of electronic all-mode regulation of crankshaft rotation frequency of the diesel engine has been developed and implemented on the motor research bench.
3. The operability of the developed electronic regulation system has been completely confirmed by studies of additional device. During tests, static and dynamic characteristics of this system have been received.
4. The dynamic mathematical model of the studied single-cylinder diesel engine supplied with the electronic regulator of rotation frequency has been developed and verified. Results of calculation with the use of this mathematical model have shown its rather high adequacy.
5. For the studied diesel, the basic matrix of fuel feeding $Bc = f(n, X)$ has been synthesized, necessary for creation of a control system on the basis of predictive model.

ACKNOWLEDGEMENTS

This project has received funding from the European Union's Horizon 2020 research and innovation programme under grant agreement No 784620.

REFERENCES

1. Furman, V.V., Ivanov V.A., & Markov, V.A. (2013). Electronic control systems for diesel engines. *Science and Innovations*, 5, 1–18. (in Russian)
2. Bogaevsky, A.B. (2001). Microprocessor system for control of rotation frequency and power of diesel-generator installation. *HGADTU Bulletin*, Kharkiv, 15–16, 153–156. (in Russian)
3. Lopez, J., Espinosa, O.J., & Agudelo, J. (2011). LQR control for speed and torque of internal combustion engines. In *8th IFAC World Congress* (pp. 2230–2235), 28 August–2 September, 2011, Milano. 10.3182/20110828-6-IT-1002.02176.
4. Payo, I., Sánchez, L., Caño, E., & Armas, O. (2017). Control applied to a reciprocating internal combustion engine test bench under transient operation: Impact on engine performance and pollutant emissions. *Energies*, *10*, 1690.
5. Lu, Y., Zhao, C., Zuo, Z., Zhang, F., & Zhang, S. (2017). Research on the common rail pressure overshoot of opposed-piston two-stroke diesel engines. *Energies*, *10*, 571.
6. Simani, S., & Bonfè, M. (2009). Fuzzy modelling and control of the air system of a diesel engine. *Advances in Fuzzy Systems*, Article ID 450259, 14. DOI:10.1155/2009/450259
7. Dong, T., Zhang, F., Liu, B., & An, X. (2015). Model-based state feedback controller design for a turbocharged diesel engine with an EGR system. *Energies*, *8*, 5018–5039.
8. Golovchuk, A.F. (2014). Universal electronic regulator for tractor diesel. *Internal Combustion Engines*, *1*, 31–34. (in Ukrainian)

ELEKTRONISKI VADĀMA DĪZEĻMOTORA STATISKO UN DINAMISKO RAKSTURLĪKŅU IZVEIDE UN IZPĒTE

P. Dumenko, S. Kravčenko, A. Prokhorenko, D. Talanin

K o p s a v i l k u m s

Dīzeļmotoru elektronisko vadības sistēmu ražojošās kompānijas aizsargā piekļuvi regulatoru algoritmu darbības programmām, kas padara praktiski neiespējamu to darbības korekciju un iestatījumu maiņu, piemēram, jauna dīzeļmotora pārbūves vai uzlabošanas gadījumos. Tāpēc ir svarīgi atzīmēt zinātniski-tehniskos šādu problēmu risinājumus, kas saistīti ar efektīvu un uzticamu sistēmu izveidi dīzeļdegvielas padeves sistēmas kontrolei ar atvērtās darba programmas algoritmu. Teorētiskajos un eksperimentālajos pētījumos par autoru izveidoto dīzeļmotora kloķvārpstas apgriezienu elektroniskās kontroles sistēmu tika konstatēta iegūto rezultātu zināma līdzība. Pētījumu gaitā tika izveidots un verificēts izpētes viencilindra dīzeļmotora, aprīkota ar elektronisko apgriezienu regulatoru, dinamiskais matemātiskais modelis.

09.01.2019.

sciendo

LATVIAN JOURNAL OF PHYSICS
AND TECHNICAL SCIENCES
2019, N 2

DOI: 10.2478/lpts-2019-0010

MODELING OF SYNERGETIC ACTION OF RADIATION AND CHEMICAL POLLUTION ON THE ENVIRONMENTAL SAFETY

N. Remez[1], A. Dychko[1], L. Yevtieieva[1], S. Kraychuk[2], N. Ostapchuk[2], J. Oliinyk[1]

[1] Institute of Energy Saving and Energy Management, National Technical University of Ukraine "Igor Sikorsky Kyiv Polytechnic Institute"
37 Peremohy Ave., Kyiv, 03056, UKRAINE

[2] Department of Economic Cybernetics, Rivne State University of Humanities
12 Stepana Bandery Str., Rivne, 33000, UKRAINE

The present paper provides a simple mathematical model that describes the synergistic interaction of environmental factors that occur in urban ecosystem. The model predicts the value of maximum synergistic action and the condition for its achievement, as well as implies the dependence of synergistic action on the intensity of the agents used and the proportion of irreversible damages after the combined effects. The developed mathematical model can be used to predict the accumulation of pollution in the ground layer of soil.

Keywords*: environmental safety, modelling, soil pollution, synergetic action*

1. INTRODUCTION

An important task of environmental safety is to study the effects caused by the combined impact of stress factors on living organisms, as well as the processes of their recovery and adaptation to stress influence. Under conditions of a polluted environment, it is important to know the features of simultaneous, synchronous effects of various harmful factors on organisms, the interaction of factors among themselves. The phenomenon of synergism in the interaction of different in nature stressors is a topical problem for many scientists.

A large number of concepts and theories of mathematical modelling of the combined action of two agents appeared in the 1970s–1990s. Semiempirical models based on the kinetic analysis of inactivation of cells to describe the simultaneous combination of ionizing radiation and hyperthermia were proposed [1], [2]. These models are tested only for the simplest cases where the survival curves are of an exponential nature.

Further development of kinetic approaches is associated with radiobiological identification of different cell states. Thus, Kappos A., Pohlit W. [3], [4] proposed the

cybernetic model of radiation inactivation of cells, which became the basis for the creation of the following models of combined effects in the studies of Brannen, Jain, Pohlit, Barendsen, Curtis, Zaider, Branner [5]–[9].

One of the visual mathematical schemes of the synergistic interaction of ionizing radiation with other factors is the molecular theory of Leenhouts and Chadwick [10], [11]. This model is used to describe the combined effect of UV and X-rays, as well as the combined action of chemical agents and ionizing radiation.

2. EXPERIMENTAL MODELLING

The goal of the research is to develop a mathematical model that describes the synergistic interaction of chemical and radiation contamination and its impact on the equilibrium state of ecosystems.

The main idea in mathematical modelling of synergistic effects is the changes in a cell under the action of ionizing radiation or other sub-damaging factor, which is not effective at its separate use but determines the degree and magnitude of the modification of radiosensitivity in a combined action, especially under conditions of uncertainty [12]–[14]. The effect of ionizing radiation is not only in the death of cells, but also in the fact that the macrocolonium, grown after irradiation and are visible, differ in size, morphology, period of appearance and frequency of "lethal sectors", i.e., the death of individual distant offsprings of the exposed cells in the process of macrocolon formation.

Let us consider the process of multiplication of cells as it is known in the theory of probability as the process of birth and death, then the following differential equation can be written for the average number of viable cells n:

$$dn/dt = \mu n - \lambda n, \tag{1}$$

where μ – the probability of cell division per unit time, λ – the probability of cell death per time unit.

For non-irradiated cells, the probability of death is small, the solution of this equation is as follows:

$$n = n_0 \exp(\mu_1 t),$$

where μ_1 – the growth rate of control cells, n_0 – the initial number of cells.

For the offsprings of irradiated cells, the probability of successful division is as follows:

$$P_i = (1 - \alpha)^i,$$

where α – the probability of failure, i.e., the failure of cell division with one damage (hit), i – the number of hits [2].

It should be noted that this connection – between the probability of successful division P and circles and the number of hits i – is similar to an exponential decrease in P with an increase in the number of hits. Consequently, the rate of reproduction of remote offsprings of irradiated cells depends on the rate of reproduction of non-irradiated cells, and on the probability of failure. Then for the offsprings of survivors after irradiation of cells with one hit, it can be written:

$$dn/dt = \mu_1(1-\alpha)n - \mu_1\alpha n. \quad (2)$$

Similar dependences can be obtained for offsprings of irradiated cells with two, three or more lesions, using the dependence of the probability of successful cells division P_i on the number of injuries i. The rate of reproduction of the offsprings of received irradiated cells and hits is written as follows:

$$\mu_i = \left[2(1-\alpha)^i - 1\right]\mu_1. \quad (3)$$

Thus, the multiplication of remote offsprings, survived after irradiation of cells, depends on both the rate of reproduction of irradiated cells and the probability of failure.

For many of the objects and effects observed in experiments by many authors, the inhibition of recovery is not due to violation of the processes of recovery. Slowing down the speed and reducing the volume of recovery are explained by a significant increase in the proportion of irreversible damages, which make the cells unable to recover. This means that the cause of synergy is not the violation of recovery processes, but the formation of irreversible damage. Additional irreversible damages can be caused by the interaction of some non-lethal sub-damages that are formed by each agent used in the combination. Therefore, it is advisable to develop a mathematical model of synergistic interaction of various agents, taking into account the interaction of sub-damages. This model should predict the dependence of the synergistic action on the ratio of "doses" of the influencing agents, the magnitude of the maximum synergistic action and the conditions for its achievement, as well as the dependence of the synergistic action on the intensity of the used agents and the proportion of irreversible damage from which the cells are unable to recover.

Synergistic interaction means that the average amount of damage per cell is greater than if the effects are summed by each agent. Thus, under the condition of synergistic interaction, some additional damage arrives. Let us assume that additional damage at combined effects is generated through the interaction of sub-damage formed after the action of each of the factors. Let us also assume that one damage from one agent interacts with one sub-damage from the other to produce one additional effective damage. Consequently, the newly created additional damage, responsible for the synergistic effect of the combined effects, is irreversible, i.e., the cells are not able to recover from such damage.

Let us also assume that each effective damage from one factor corresponds to p_1 sub-damage induced by this factor. Similarly, let us introduce the second parameter p_2 – the amount of sub-damage induced on one effective damage from the second factor. Then, assuming that the amount of effective (for example, lethal) damage

induced by the first factor is N_1 and the second – N_2, then the total amount of sub-damage generated by the first factor is equal to p_1N_1 and the second – to p_2N_2. Then the additional amount of effective N_3 sub-damage is determined by the expression:

$$N_3 = \min\{p_1N_1; p_2N_2\}. \quad (4)$$

Hence, the total amount of lethal damage N_Σ with the combined effect of two factors is as follows:

$$N_\Sigma = N_1 + N_2 + N_3 = N_1 + N_2 + \min\{p_1N_1; p_2N_2\}. \quad (5)$$

The coefficient of synergistic action, which shows the ratio of the amount of effective damage in the case of a combined action to the amount of damage, expected in the sum of damage, formed by each agent, can be written in the form:

$$k = \frac{N_1 + N_2 + \min\{p_1N_1; p_2N_2\}}{N_1 + N_2}. \quad (6)$$

This expression describes quantitively the magnitude of synergistic action. If $p_1N_1 < p_2N_2$, i.e., cells die mainly from the action of the second factor, $\min\{p_1N_1; p_2N_2\} = p_1N_1 \min\{p_1N_1; p_2N_2\} = p_1N_1$, and then from equation (6):

$$k_1 = 1 + \frac{p_1}{(1 + N_2/N_1)}. \quad (7)$$

$$p_1 = (k_1 - 1) \cdot (1 + N_2/N_1). \quad (8)$$

Similarly, if cells die primarily from the action of the first factor, i.e., $p_1N_1 > p_2N_2$ and

$$\min\{p_1N_1; p_2N_2\} = p_2N_2,$$

$$k_2 = 1 + \frac{p_2}{(1 + N_1/N_2)}. \quad (9)$$

$$p_2 = (k_2 - 1) \cdot (1 + N_1/N_2). \quad (10)$$

Equation (6) can be rewritten in the next form:

$$k = 1 + \frac{\min\{p_1; p_2 N_2/N_1\}}{(1 + N_2/N_1)}. \quad (11)$$

It is obvious that the maximum synergistic effect occurs with the maximum value of the expression $\min\{p_1; p_2 N_2/N_1\}/(1 + N_2/N_1)$.

Figure 1 presents the graphs of the dependencies of the functions $f_1 = 1 + p_1/(1 + N_2/N_1)$ and $f_2 = 1 + p_2 \cdot N_2/N_1/(1 + N_2/N_1)$ on the ratio of effective damage N_2/N_1 formed by each agent used in the combination. These functions are calculated for arbitrarily selected values p_1 and p_2 ($p_1 = 3$, $p_2 = 2$).

From Fig. 1 it can be seen that f_1 decreases and f_2 increases with an increase in N_2/N_1, and the maximum synergistic action is obtained at $f_1 = f_2$, i.e.,

$$\frac{p_1}{1 + N_2/N_1} = \frac{p_2 \cdot N_2/N_1}{1 + N_2/N_1}. \quad (12)$$

After some mathematical transformations, a condition for achieving maximum synergistic interaction is obtained:

$$p_1 \cdot N_1 = p_2 \cdot N_2. \quad (13)$$

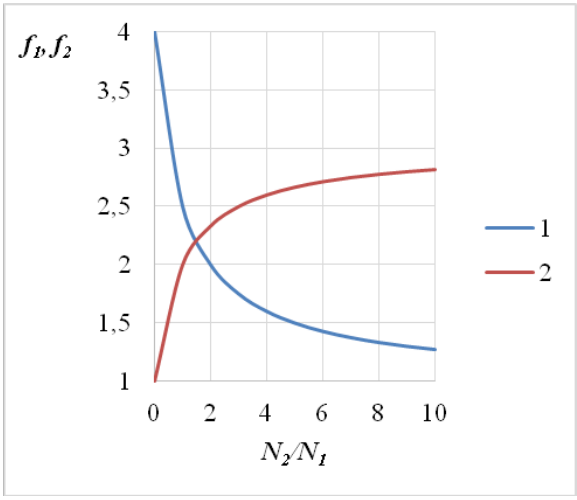

Fig. 1. Calculated dependencies of functions f_1 (1) and f_2 (2) on the ratio N_2/N_1 for arbitrarily selected parameters $p_1 = 3$, $p_2 = 2$.

This means that maximum synergy effect is achieved when both agents form equal amount of sub-damage. If the values of p_1 and p_2 do not differ much from one another, maximum synergy is achieved at approximately the same contributions of each agent in the researched effect. Equation (13) can be rewritten as follows:

$$N_2/N_1 = p_1/p_2. \quad (14)$$

Ratio N_2/N_1 can be estimated from the dose-effect curve slope ratio, for example, after the action of chemical contamination ($1/t_2$) and radiation contamination ($1/t_1$), where t_1 and t_2 – the duration of a separate action of radiation and chemical contamination that reduces survival cells in e times (e – the basis of natural logarithms) on the exponential sections of the dose-effect curves, i.e.:

$$N_2/N_1 = t_1/t_2. \quad (15)$$

Equations (13)–(15) determine the conditions for achieving maximum synergistic interaction. Taking into account equations (6) and (4), the value of the maximum coefficient of synergistic interaction can be represented as follows:

$$k_{max} = 1 + \frac{p_1 \cdot p_2}{p_1 + p_2}. \quad (16)$$

As can be seen from equation (16), k_{max} is completely determined by the values of p_1 and p_2 and does not depend on N_1 and N_2. Thus, it is possible to predict the maximum synergistic effect (16) and the ratio N_2/N_1 (13) at which it is achieved.

Using equations (8) and (10), as well as the corresponding experimental values of the synergistic amplification coefficients from two independent experiments of the combined effect, the basic parameters of the model p_1 and p_2 can be determined as the amount of sub-damage occurring in one effective damage from the agents used. Then, using equation (6), the synergistic gain for all values of N_1 and N_2 can be calculated, and by equations (13) and (16) – the maximum value of the synergistic gain and the condition in which it is achieved.

On the basis of the above-described principles of mathematical modelling of the synergistic action of several factors, a mathematical model of the effect of synergistic action of radiation and chemical pollution on the stability of ecosystems is developed, which has the following form:

$$\begin{cases} \frac{dN_1}{dt} = p_1 N_1 - \frac{p_1}{K_1} N_1^2 + k_1 N_1 N_2, \\ \frac{dN_2}{dt} = p_2 N_2 - \frac{p_2}{K_2} N_2^2 + k_2 N_1 N_2, \end{cases} \quad (17)$$

where N_1 – the dose of radiation, mSv/year; N_2 – the concentration of harmful substance, mg/kg; p_1, p_2 – constants of the rate of accumulation of pollution determined experimentally; K_1 – the magnitude of radioecological capacity, mSv/year; K_2 – the value of the extremely permissible concentration (EPC) of the harmful substance, mg/kg; k_1, k_2 – coefficients of synergy for each component.

3. RESULTS AND DISCUSSION

The developed mathematical model is used to predict the synergistic effect of the ecosystem pollution in the city of Mariupol, Ukraine. Data from the Ukrainian Central Geophysical Observatory on contamination by heavy metals of soils in Mariupol in 2014–2017 (Table 1) and data from the Mariupol Hydrometeorological Observatory on the radiation background of Mariupol in 2014–2017 (Table 2) were used for calculations.

Table 1

The Content of Heavy Metals in the Soils of Mariupol in 2014–2017

Year	Pollutants (average / maximum, in multiplicity to norms)			
	Cu	Pb	Zn	Cd
2014	0.4 / 4.2	1.7 / 6.5	1.5 / 4.9	0.1 / 0.8
2015	1.0 / 3.3	3.5 / 36.2	3.3 / 7.3	0.8 / 2.5
2016	1.7 / 5.6	4.1 / 13.1	4.9 / 10.0	1.8 / 3.5
2017	0.9 / 3.5	1.3 / 8.4	2.9 / 5.6	2.2 / 14.5

Table 2

Radiation Background of Mariupol in 2014–2017

	2014	2015	2016	2017
Cs, mSv/year	1.052	1.227	1.14	0.964

After the calculations, the results as graphic dependences for cesium-137 with copper, lead, zinc and cadmium were obtained (Figs. 2–5).

The figures show that the maximum synergistic effect is achieved at approximately the same contributions of each agent in the studied effect.

The greatest harmful effect on environment among the studied heavy metals is synergistic interaction of cesium-137 and cadmium, since the maximum synergy

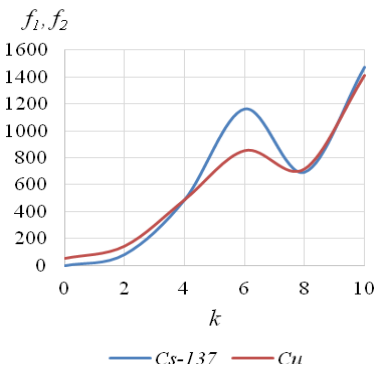

Fig. 2. Synergistic effect of *Cs* and *Cu*.

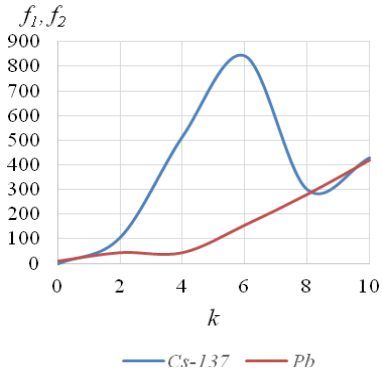

Fig. 3. Synergistic effect of *Cs* and *Pb*.

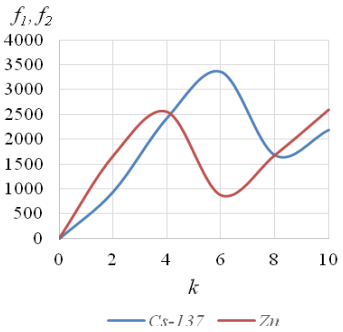

Fig. 4. Synergistic effect of *Cs* and *Zn*.

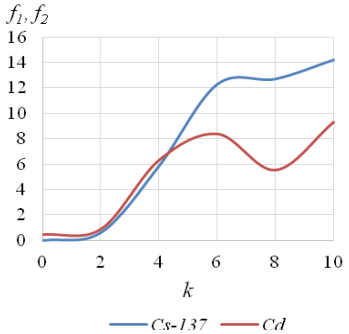

Fig. 5. Synergistic effect of *Cs* and *Cd*.

value is achieved when the cadmium EPC is exceeded by only 5 %. The next by harmfulness for the environment is the synergistic interaction of cesium-137 and copper in excess of copper EPC by 20 % and cesium-137 with lead – by 26.7 %. The least harmful among these interactions is the synergistic interaction between cesium-137 and zinc, which is achieved when the EPC is exceeded by 230 %.

4. CONCLUSIONS

The present study has introduced the developed mathematical model that describes the synergistic interaction of environmental factors that occur in the biosphere. The model predicts the value of maximum synergistic action and the condition for its achievement, as well as implies the dependence of synergistic action on the intensity of the agents used and the proportion of irreversible damages after the combined effects.

The authors of the research have developed the mathematical model used for the analysis of environmental pollution of the city. It has been established that the maximum synergistic effect is achieved at approximately the same contributions of each agent in the studied effect.

The obtained results show that the greatest harmful effect on the environment among the studied heavy metals is synergistic interaction of cesium-137 and cadmium, since the maximum synergy value is achieved with only 5 % excess of cadmium EPC.

REFERENCES

1. Trujillo, R., & Dugan, V. (1972). Synergistic inactivation of viruses by heat and ionizing radiation. *Biophis*. *J. 12*, 92–113.
2. Reynolds, M.C., & Brannen, J.P. (1973). Thermal enhancement of radiosterilization. In *Radiation Preservation of Food* (pp. 165–176). Vienna: International Atomic Energy Agency.
3. Kappos, A., & Pohlit, W. (1972). A cybernetic model for radiation reactions in living cells. I. Sparsely ionizing radiations; stationary cells. *Int. J. Radiat. Biol. 22*, 51–65.
4. Pohlit, W., & Drenkard, S. (1985). Quantitative determination of the contribution of indirect and direct radiation action to the production of lethal lesions in mammalian cells. *Radiation Protection Dosimetry*, *13*(1-4), 195–198.
5. Brannen, J.P. (1975). A temperature- and dose rate-dependent model for the kinetics of cellular response to ionising radiation. *Radiat. Res.*, *62*(3), 379–387.
6. Jain, V., & Pohlit, W. (1986). Biocybirnetics of Cancer. *Optimizing Cancer Treatment with Ionizing Radiations*. Banglore: INSDOC.
7. Barendsen, G.W. (1992). Interaction of the LET dependence of radiation induced lethal and sublethal lesions in mammalian cells. *Biophysical Modelling of Radiation Effects*, 13–20.
8. Curtis, S.B. (1992). Application of the LPL model to mixed radiations cells. *Biophysical Modelling of Radiation Effects*, 21–28.
9. Zaider, M., & Branner, D. (1992). The application of the principle of “dual radiation action” in biophysical modelling cells. *Biophysical Modelling of Radiation Effects*, 37–46.

10. Leenhouts, H.P., & Chadwick, K.H. (1978). An analysis of synergistic sensitization. *Brit. J. Cancer*., *37*, 198–201.
11. Chadwick, K.H., & Leenhouts, H.P. (1981). *The molecular theory of radiation biology*. Berlin-Heidelberg-New York: Springer Verlag.
12. Remes, N.S., & Oliinyk Y.S. (2017). Mathematical modeling of the effect of synergistic action of chemical and radiation pollution on the stability of ecosystems. In *Power Engineering. Ecology. Man*. Kyiv, Ukraine: NTUU "KPI".
13. Dychko, A., Yevtieieva, L., & Guzovsky, M. (2014). Quality management of the environment. In *Actual Problems of Management in the Modern Globalization Process*. Irpen, Ukraine: National University of State Tax Service of Ukraine.
14. Dychko, A., & Yeremeev, I. (2016). Problem of uncertainty in environmental monitoring. *Systems of Information Processing*, *6*, 45–47.

RADIĀCIJAS UN ĶĪMISKĀ PIESĀRŅOJUMA SINERĢISKĀS IEDARBĪBAS MODELĒŠANA UZ VIDES DROŠĪBU

N. Remezs, A. Dičko, L. Jevtejeva, S. Kraičuks, N. Ostapčuks, J. Olinik

K o p s a v i l k u m s

Rakstā sniegts vienkāršs matemātisks modelis, kas apraksta pilsētas ekosistēmā sastopamo vides faktoru sinerģisko mijiedarbību. Modelis prognozē maksimālās sinerģiskās darbības vērtību un tās sasniegšanas nosacījumu, kā arī sinerģiskās darbības atkarību no izmantoto aģentu intensitātes un neatgriezenisko bojājumu proporciju pēc kombinētās ietekmes. Izstrādāto matemātisko modeli var izmantot, lai prognozētu piesārņojuma uzkrāšanos augsnes slānī.

21.11.2018.

sciendo

LATVIAN JOURNAL OF PHYSICS
AND TECHNICAL SCIENCES
2019, N 2

DOI: 10.2478/lpts-2019-0011

ELECTRONICS

EXPERIMENTAL MEASUREMENT OF ERBIUM-DOPED OPTICAL FIBRE CHARECTERISTICS FOR EDFA PERFORMANCE OPTIMIZATION

I. Lavrinovica, A. Supe, J. Porins
Riga Technical University
Institute of Telecommunications,
12 Azenes Str., Riga, LV-1048, LATVIA
e-mail: ingrida.lavrinovica_1@rtu.lv

The paper presents experimental study of the major erbium-doped fibre amplifier **(**EDFA) features such as gain at low signal and gain saturation by an application of different erbium-doped optical fibres (EDFs). The main objective of the research is to estimate how the performance of EDFA varies depending on the length of doped fibre, pumping configuration scheme, as well as excitation source power. It is shown that a high gain coefficient of 16–20 dB can be practically achieved.

Keywords: *erbium-doped fibre amplifier, gain coefficient, gain saturation, rare earth doped fibres, pump power*

1. INTRODUCTION

Significant growth of traffic intensity and increase of data transmission rates in fibre optic transmission systems (FOTS) require higher optical signal-to-noise ratio (SNR) and bit error ratio (BER), which inevitably increase as signal propagates along the optical fibre [1], [2]. Typical fibre loss around the 1550 nm wavelength is about 0.2 dB/km and as the distance increases to 100 km, signal is attenuated by 20 dB. Respectively, optical power depletion affects the performance of transmission systems and in this case, development of optimised optical amplifiers is required.

In today's FOTS, erbium-doped fibre amplifier has been widely used for amplification of signals in wavelength division multiplexed systems. The primary EDFA component is a glass optical fibre doped with Er^{3+} ions (typically in the region of 100 to 500 ppm) and pumping light source. When a beam of light carrying signals passes the erbium-doped optical fibre, a pump laser provides the amplifier energy at erbium absorption peaks of 980 and/or 1480 nm. It has several advantages: immunity to crosstalk among wavelength-multiplexed channels, insensitivity to light polarization state and high pump power utilissation (conversion into signal amplification up to 50 %). However, the presence of major drawback such as an

influence of amplified spontaneous emission (ASE), limited gain bandwidth and non-uniformity of a gain curve requires a solution aimed at the improvement of EDFA performance.

Preliminary analytical studies have shown that the performance improvement of the EDFA should be guided by the optimal benchmark against the effectiveness of the gain. This optimal criterion includes the combination of an erbium-doped fibre (EDF) and pump source power, which would ensure a maximal gain coefficient with a minimal noise factor. Moreover, the solution must also be beneficial in terms of energy efficiency, i.e., maximising the gain for a given available pump power and minimising the needed pump power for a desired gain [4]. In present study, we have investigated the performance of EDFA experimentally by using different erbium-doped fibre samples of two manufacturers. Since operating of doped-fibre amplifier depends on fibre geometrical parameters, such as core and cladding properties, absorption and emission coefficients as well as fibre numeric aperture (NA), it is crucial to investigate how they affect EDFA characteristics.

2. METHOD ANALYSIS

EDFA gain is implemented when the amplifier is optically pumped to achieve population inversion of erbium ions at the excited state versus ground state. Gain coefficient depends not only on the wavelength of the incident signal, but also on the local beam intensity at any point inside the amplifier. Considering the case with the gain medium model as a homogeneously broadened two-level system, the gain coefficient can be written as follows:

$$g(\omega) = \frac{g_0}{1 + (\omega - \omega_0)^2 T_2^2 + \frac{P}{P_s}}, \tag{1}$$

where g_0 is the peak value of the gain, ω is the optical frequency of the incident signal, is the atomic transition frequency, and P is the optical power of the signal being amplified. The saturation power P_s depends on the parameters of the rare-earth element used, such as population relaxation time T_1 (it varies in the range of 100 ps–10 ms depending on the media) and the transition crosssection; T_2 is known as the dipole relaxation time and is typically quite small (< 1 ps).

In the unsaturated regime when $P/P_s \ll 1$ throughout the amplifier by neglecting the term P/P_s in (1), gain coefficient becomes

$$g(\omega) = \frac{g_0}{1 + (\omega - \omega_0)^2 T_2^2} . \tag{2}$$

Respectively, the gain is maximal when the incident frequency ω coincides with the atomic transition frequency ω_0. The amplifier gain G known as the amplification factor shows the relationship between the continuous-wave (CW) signal input power P_{in} and output power P_{out}:

$$G = \frac{P_{in}}{P_{out}}; \tag{3}$$

$$gP = \frac{dP}{dz}, \tag{4}$$

where $P(z)$ is the optical power at a distance z from the input end. A straightforward integration with the initial condition $P(O) = P_{in}$ shows that the signal power grows exponentially as follows:

$$P(z) = \exp(gz). \tag{5}$$

Both $g(\omega)$ and $G(\omega)$ are at maximum when the frequency is at resonance $\omega = \omega_0$ and decrease when the frequency is detuned from resonance. However, the amplifier factor G decreases much faster than the gain coefficient g. Practically, gain coefficient is denoted as G and calculated as the ratio between P_{in} and P_{out}.

In the gain saturation region, the signal growth is linear. This occurs when the signal intensity I_s field grows to a large value comparable to saturation intensity field I_{sat}. The signal growth is then damped by the saturation factor:

$$\frac{1}{1+\frac{I_s}{I_{sat}}}. \tag{6}$$

The ratio of I_s and I_{sat} becomes large compared to unity $I_s/I_{sat} \gg 1$. The growth of signal in the saturation region is determined by:

$$\frac{dI_s}{dz} = I_{sat}\left(\frac{I_p-1}{I_p+1}\right)\sigma_s N, \tag{7}$$

where I_p is a pump intensity field, N is a population inversion, σ_s is a signal absorption and emission crosssection. I_{sat} is linearly dependent on pump power, when signal saturation varies with pump power. The saturation output power is inversely proportional to emission crosssection of fibre; it causes the saturation power being higher at 1550 nm than at 1530 nm [3].

3. EXPERIMENTAL SETUP

Taking into account the simulation results from our previous studies on EDFA mentioned in [5] and [6], practical experiments were carried out using co-pumping and bidirectional pumping scheme to determine an optimal combination of the doped-fibre length and excitation source power that could be used to improve EDFA characteristics. Experiments focused on evaluating EDFA low signal gain and gain saturation. Low signal gain criteria were chosen since the EDFA had a nonlinear nature and measurement of the large-signal saturating gain might not completely characterise the amplifier.

The first part of the experiment represents co-pumping EDFA configuration and the relevant experimental scheme is shown in Fig. 1. Continuous-wave laser operates at the wavelength of 980 nm (maximum power 80 mW) and ensures pumping at 1550 nm. Optical isolators reduce reflections at the input to the amplifier and lowpass filter limits the transmission of amplified spontaneous emission (ASE) frequency components.

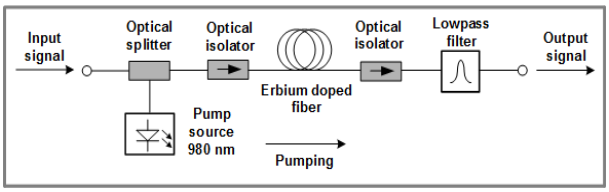

Fig. 1. EDFA experimental scheme with co-pumping configuration.

Measurements were performed with two types of erbium doped-fibres intended for the C optical band: FIB-1 (samples of 5m and 15m) and FIB-2 (sample length 12m). The gain coefficient is introduced as the maximum ratio between the small signal gain (in decibels) and the launched pump power (in milliwatts). The usage of different sample lengths is mandatory as it shows more precise dynamic of stimulated emission process. Input signal power was set to 13.2 dBm and it was constant for all the measurements. General parameters for mentioned fibres are listed in Table 1.

Table 1

Parameter List of the Used Erbium-doped Fibres

Parameter	**FIB-1**	**FIB-2**
Absorption coefficient at 1530 nm	5.45 dB/m	7.5 dB/m
Absorption coefficient at 1480 nm	2.4 dB/m	2.8 dB/m
Cut-off wavelength	942 nm	1014 nm
Attenuation at 1200 nm	2.8 dB/km	< 10 dB/km
Primary cladding diameter	125 +/- 1 µm	125 +/- 1 µm
Secondary cladding diameter	245 +/- 10 µm	245 +/- 10 µm
Core radius	4.1 µm	3.2 µm
Numerical aperture (NA)	0.22	0.26

Excitation source power was obtained through middleware measurements by changing the current level of 980 nm pump module since EDF samples used in experiments were with different erbium ion concentration. Pump power values used in low signal gain evaluation are from 21.1 mW to 54.1 mW.

The second experiment was done with bidirectional pumping scheme (Fig. 2) where two light sources were used. Those sources ensure simultaneous pumping in opposite directions: the one at 1480 nm with high quantum efficiency operates in counter-propagating regime, while 980 nm source in co-propagating regime. Input signal power for 980 nm pumping source remains the same and is 13.2 dBm respectively but for 1480 nm it is fixed at 11.2 dBm. Moreover, in the present experiment we also used 2m and 5m long erbium-doped fibre samples from another manufacturer (FIB-3). The relevant parameters of FIB-3 are shown in Table 2.

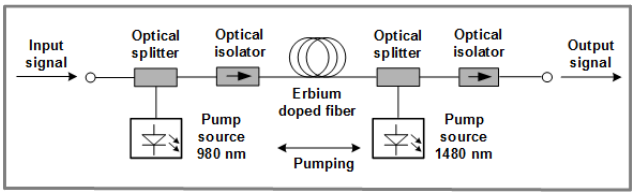

Fig. 2. EDFA experimental scheme with bidirectional pumping configuration.

Table 2

Parameter List of the Used FIB-3 Sample

Type of the fibre	I-12 (980/125)
Absorption coefficient at 979 nm	11.2 dB/m
Attenuation at 1200 nm	4.3 dB/km
Secondary cladding diameter	239.2 μm
Core radius	0.1 μm
Cut-off wavelength	950 nm
Primary cladding diameter	124.8 μm
Mode field diameter	6.1 μm
Numerical aperture (NA)	0.22

4. RESULTS AND DISCUSSION

Figure 3 represents the dynamics of low signal gain using FIB-1 and FIB-2 samples with co-pumping EDFA configuration. It can be seen that gain coefficient variations are negligible since with an increase in pump power it changes only for 1–2 dB. As may be seen below, from the energy efficiency perspective it is optimal to use 12m long FIB-2 when the gain of 17.1 dB is achieved at 37.4 mW. It was also observed that the usage of 15m long FIB-1 led to a faster reach of EDFA saturation regime: after an increase in pump power by about 8 mW (from 46.2 to 54.1 mW), the gain coefficient changed by 0.8 dB. The overall measurement results using co-pumping EDFA scheme showed that the maximal gain coefficient of 19.1 dB corresponded to pump power of 54.1 mW.

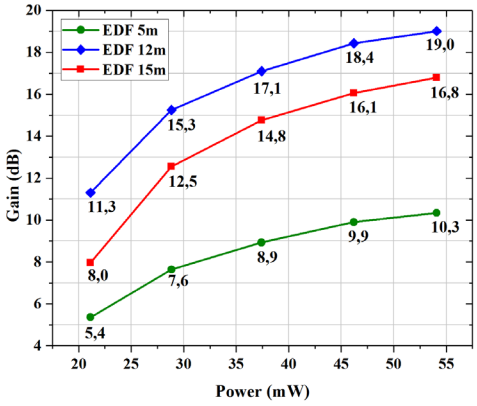

Fig. 3. EDFA gain at a low signal for 5m (FIB-1), 12m (FIB-2) and 15m long (FIB-1) using co-pumping configuration.

In theory, bidirectional EDFA pumping should increase both output power and gain coefficient. After an analysis of the obtained results using a bidirectional pumping scheme, this statement was practically proven. The results for 15m long FIB-1 (Fig. 4) show that the minimal pump power of 21.3 mW corresponds to the gain coefficient of 14.4 dB. In comparison with the single-direction pumping scheme, it is a notable benefit since the previously mentioned gain coefficient required pump power of 37.4 mW. From this observation, it can be clearly seen that the application of bidirectional pumping leads to energy preservation by up to 16 mW. Maximal gain coefficient for 15m and 20m long samples is in the range of 19–20 dB.

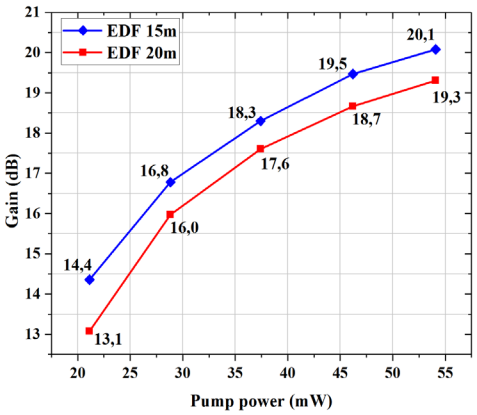

Fig. 4. EDFA gain at a low signal for 15m and 20m long FIB-2 using bidirectional pumping configuration.

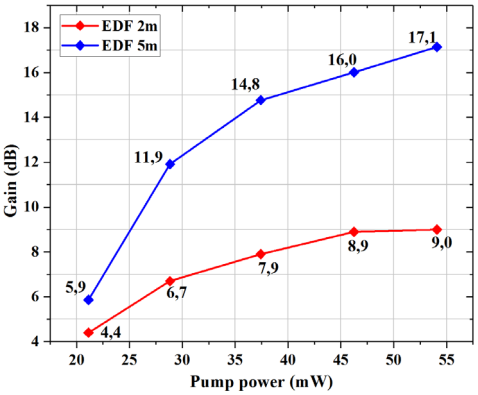

Fig. 5. EDFA gain at a low signal for 2m and 5m long FIB-3 samples using bidirectional pumping configuration.

The usage of FIB-3 erbium-doped fibre with bidirectional EDFA configuration (Fig. 5) gives a maximal gain coefficient of 9 dB with 2m long EDF at pump power of 46.2 mW. With an increase in fibre length to 5 m, maximal gain increment is 7.2 dB. Summing up the results for both FIB-3 samples, it can be concluded that present fibres are suitable for an optimised EDFA design since short lengths are preferable from the construction perspective.

Gain saturation is experienced when the metastable energy level population is severely depleted by a high rate of stimulated emission. Consequently, as the input signal power is increased past the low-signal region, more photons will enter the erbium-doped fibre stimulating emission of photons and depleting the metastable energy level faster than it can be filled. Therefore, the amplification will reach a saturation limit and with the growth of input signal power the gain will decrease. The relevant gain saturation measurement results are depicted in Figs. 6 and 7.

When comparing the results for FIB-1 of 5m and 15m (Fig. 6) by maximal achievable coefficient, it is seen that the usage of a longer fibre does not affect gain indicators since the maximum value differs only by 1 dB: 19.8 dB for 15m and 18.3 dB for 5m, respectively. However, from the energy efficiency perspective the usage of 5m fibre is more effective as the maximum gan is achieved with the power of 3.3 mW. For a 15 m long sample pump power states to 4.6 mW. In the case of Fibrecore EDF-s (Fig. 7), the greatest gain values of 18.5 and 21.2 dB correspond to 2 m and 5 m long fibres. The relevant pump source powers, where the most active stimulated emision process is observed, are at 3.4 and 6.3 mW.

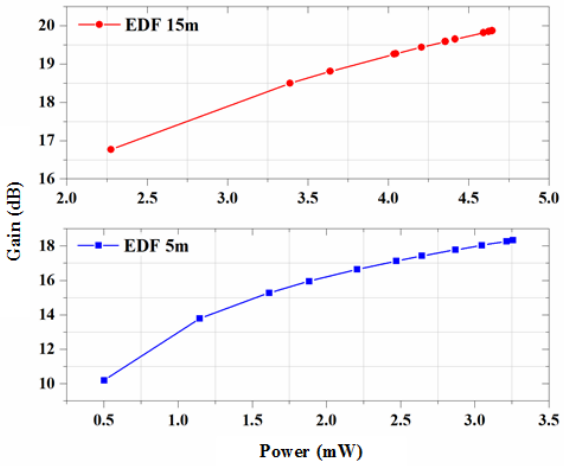

Fig. 6. Gain saturation for 15m and 5m long FIB-1 samples.

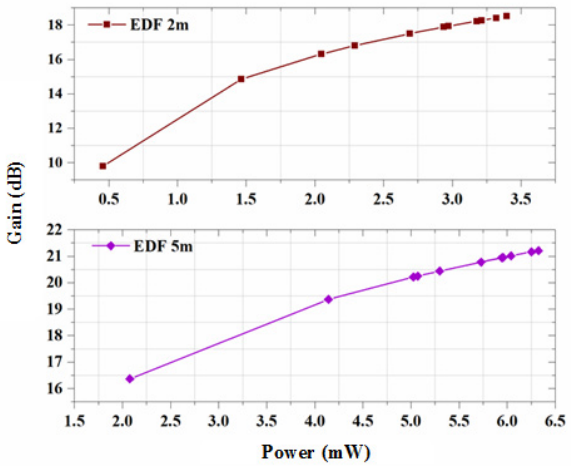

Fig. 7. Gain saturation for 2m and 5m long FIB-3 samples.

5. CONCLUSIONS

In the present study, the major erbium-doped fibre amplifier features, such as gain at a low signal and gain saturation by the application of different erbium-doped optical fibres, have been experimentally evaluated.

The obtained results have shown that the usage of 15m long FIB-1 leads to a faster reach of EDFA saturation regime: after an increase in the pump power by about 8 mW (from 46.2 to 54.1 mW), the gain coefficient has changed by 0.8 dB. The present findings are of direct practical relevance.

It has been demonstrated that the application of bidirectional pumping setup where 1480 nm light source operates at counter-propagating direction and 980 nm source at co-pumping direction, respectively, allows achieving a higher low-signal gain with less power consumption. Overall, the maximal gain achieved with 15m and 20m long FIB-1 samples is in the range of 19–20 dB.

In conclusion, during this study we have obtained the optimal range of doped fibre length (5–20m), which makes it possible to provide the gain within 16–20 dB at the pump power of 54 mW. Further research will be focused on simulations and experimental analysis of other rare-earth dopants and their application in optical signal amplification solutions.

ACKNOWLEDGEMENTS

The research has been supported by the European Regional Development Fund within the Activity 1.1.1.2 "Post-doctoral Research Aid" of the Specific Aid Objective 1.1.1 "To increase the research and innovative capacity of scientific institutions of Latvia and the ability to attract external financing, investing in human resources and infrastructure" of the Operational Programme "Growth and Employment" (No. 1.1.1.2/VIAA/1/16/151).

REFERENCES

1. Supe, A., Porins, J. & Ivanovs, G. (2013). Optical fibre nonlinear coefficient measurements using FWM. In *Progress in Electromagnetics Research Symposium (PIERS) Proceedings*, 25–28 March 2013 (pp. 339–341). Taiwan, Taipei.
2. Miyamoto, Y., & Takenouchi, H. (2014). Metro dense space-division-multiplexing optical communications technology for petabit-per-second class transmission. *NTT Technical Review Regular Articles*. 1–7.
3. Agrawal, G.P. (1997). *Fibre-optic communication systems.* New York: John Wiley & Sons.
4. Essiambre, R.J., Kramer, G., Winzer, P.J., Foschini, G.J., & Goebel, B. (2010). Capacity Limits of Optical Fibre Networks. *J. Lightwave Technol., 28*, 662–701.
5. Lavrinovica, I., Porins, J., & Ivanovs, G. (2015). Estimation of EDFA performance in 40 Gbit/s 8 channel DWDM transmission system. In *Progress in Electromagnetics Research Symposium (PIERS) Proceedings*, 6–9 July 2015 (pp. 502–505). Prague, Czech Republic.

6. Lavrinovica, I., & Porins, J. (2015). Noise figure analysis of EDFA with different pumping configurations in 40 Gbit/s 8 channel DWDM transmission system. In *Advances in Wireless and Optical Communications (RTUWO) Proceedings*, 5–6 November 2015 (pp. 1–4). Riga, Latvia.

AR ERBIJU LEĢĒTO OPTISKO ŠĶIEDRU RAKSTURLIELUMU EKSPERIMENTĀLIE MĒRĪJUMI EDFA PASTIPRINĀTĀJA DARBĪBAS OPTIMIZĀCIJAI

I. Lavrinoviča, A. Supe, J. Poriņš

K o p s a v i l k u m s

Mūsu darbā tika eksperimentāli pētītas ar erbiju leģēto optisko šķiedru pastiprinātāja (EDFA) pamatīpašības, tādas kā spēja pastiprināt vājos signālus un pastiprinājuma efektivitāti, izmantojot dažāda garuma ar erbiju leģēto optisko šķiedru (EDF) paraugus. Pētījuma mērķis bija novērtēt EDFA darbību atkarībā no leģētās šķiedras garuma, pumpēšanas konfigurācijas un ierosinošā avota jaudas. Mērījumos tika izmantotas trīs dažādas EDF šķiedras no diviem ražotājiem: FIB-1 (garumi 5m, 15m un 20m) , FIB-2 (garums 12m) un FIB-3 (garumi 2m un 5m). Ierosinošā avota jaudas diapazons ir no 21.1 mW līdz 54.1 mW.

Noteikts, ka vāja signāla pastiprināšanas režīmā ar divvirzienu pumpēšanu 15m garai FIB-1 šķiedrai pie minimālas ierosinošā avota jaudas 21.3 mW atbilst 14.4 dB pastiprinājums. Tas nodrošina 16 mW jaudas ietaupījumu salīdzinājumā ar vienvirziena pumpēšanu, kur šādu pastiprinājuma koeficientu iegūst ar jaudu 37.4 mW. Mērījumu rezultātā iegūti optimālie EDF šķiedru garumi (5-20m) ar kuriem iespējams nodrošināt pastiprinājumu 16-20 dB robežas pie ierosinošā avota jaudas līdz 54 mW.

25.02.2019.

sciendo

LATVIAN JOURNAL OF PHYSICS
AND TECHNICAL SCIENCES
2019, N 2

DOI: 10.2478/lpts-2019-0012

INVESTIGATION OF EDFA PERFORMANCE IN DWDM TRANSMISSION SYSTEMS UNDER DIFFERENT OPERATING CONDITIONS

J. Putrina, S. Olonkins, V. Bobrovs, J. Porins
Institute of Telecommunications, Riga Technical University
12 Azenes Str., Riga, LV-1048, LATVIA
Sergejs.olonkins@rtu.lv

The article investigates dependence of EDFA performance on its operating conditions. First of all, the impact of changes in channel spacing on the quality of the amplifier signal and on the desired EDFA configuration is observed – three different values of channel spacing are considered – 37.5 GHz, 50 GHz and 100 GHz. Afterwards, the impact of EDFA positioning on the quality of the amplified signal and the desired configuration is assessed. Three different EDFA positioning scenarios are considered – when the EDFA is used as a power booster, as an in-line amplifier and as a preamplifier. In all cases, such configuration of the EDFA is found that can ensure bit-error ratio (BER) values below $1 \cdot 10^{-9}$ in all channels of the system. To assess the performance of the amplifiers, power penalty values are obtained in respect to identical transmission systems but without amplification.

Keywords: *Amplifier positioning, channel spacing, erbium-doped fiber amplifiers, wavelength division multiplexing.*

1. INTRODUCTION

The throughput of fibre optical transmission systems has experienced a significant increase during the past decades. This tendency is mostly driven by the all-time growing popularity and availability of online multimedia services and machine-to-machine applications. According to the Cisco virtual networking index forecast, it is expected that monthly global IP traffic will reach 396 Exabytes till the end of 2022 [1]. Huge effort is made to increase the throughput of future optical networks and to improve performance of the existing transmission systems. The two most common ways of increasing capacity of existing wavelength division multiplexed (WDM) transmission systems is to increase the bit rate per channel or to ensure simultaneous transmission of a higher number of channels [2], [3].

Implementation of any of the two above-mentioned approaches results in stricter requirements for the quality of the transmitted signal in WDM systems. At this point, optimisation of performance of optical amplifier becomes curtail, as this network element is the main source of optical signal impairments. Erbium-doped fibre amplifiers (EDFAs) are the most frequently used type of amplifiers in modern

optical networks, as they operate in the wavelength region where minimal optical signal attenuation is observed (1530–1565 nm) in standard single mode fibres, and as they are relatively easy to build. EDFAs are also known for their high energy transfer efficiency (> 50 % of pump energy is used for excitation of Er^{+3} ions), almost complete polarization insensitivity and relatively low noise characteristics [4], [5].

Performance of EDFAs is highly dependent on such amplifier parameters as erbium-doped fibre (EDF) length, pump power, pump wavelengths and pump propagation direction. These parameters have direct impact on the achieved level of population inversion in the gain medium, and, therefore, incorrect choice of at least one of these parameters will lead to changes in the shape of the gain spectrum, the achieved level of amplification and on the amount of produced amplified spontaneous emission (ASE) noise [6], [7]. Furthermore, the performance of the amplifier is also highly dependent on the conditions in which the amplifier is operating. Any adjustments in system configuration that will lead to changes in input signal power or the width of the wavelength band to be amplified will impact the total system performance as well as the configuration of the EDFA that would be optimal for the system under attention [5], [8].

The goal of this article is to investigate how changes of channel spacing and of input signal power influence the performance of Erbium-doped fibre amplifiers. While choosing EDFA configuration for every system setup, the aim is to find the lowest pump power that will ensure the required quality of the signal in order to avoid excessive pumping, which may result in additional amplified signal discrepancies.

2. INVESTIGATION OF CHANNEL SPACING IMPACT ON EDFA PERFORMANCE IN WDM TRANSMISSION SYSTEMS

The gain spectrum of EDFAs is strictly wavelength dependent due to the molecular structure of the Erbium doped fibre; its width is limited approximately to 40 nm for conventional EDFAs. As there is a need to increase the capacity of WDM transmission systems, the obvious solution of enhancing the total transmission speed of existing systems with EDFAs is to decrease channel spacing in order to ensure simultaneous transmission of a larger number of channels over the limited gain bandwidth. Changes in channel spacing may have direct impact on the performance of the whole system and, therefore, after such changes re-adjustment of amplifier parameters is required in order to find the most suitable EDFA configuration for the system under attention. The goal of this section is to assess the impact of changing channel spacing in a WDM transmission system on the performance of EDFAs.

OptSim 5.2 simulation software was used to obtain the results introduced in this article. As experience shows, it is capable of handling complex simulations of multichannel optical transmission systems and of ensuring high accuracy results without high performance requirements for the hardware it is operating on [9]–[11]. In order to assess the impact of channel spacing on the performance of EDFAs, a simulation model of a 9.953 Gbps WDM transmission system with non-return to zero intensity on-off keying modulation (NRZ-OOK) transmission distance of 150 km and an in-line EDFA introduced. This simulation model is shown in Fig.1.

Each transmitter consists of a data source, NRZ coder and a continuous wave laser, the 6 dBm output radiation of which is modulated by an external Mach-Zehnder modulator. Each transmitter operated at its own frequency, dependent on the channel spacing used in the system. Three different channel spacing values are observed: 37.5 GHz, 50 GHz and 100 GHz. The centre frequencies of the 16 transmitters are distributed throughout the following frequency ranges: from 193.1 to 193.6625 THz (37.5 GHz channel spacing), from 193 THz to 193.75 THz (50 GHz channel spacing) and from 192.6 to 194.1 THz (100 GHz channel spacing).

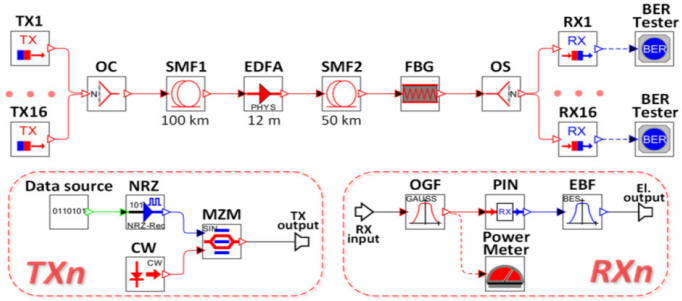

Fig. 1. Simulation model of 16 channel 9.953 Gbit/s WDM transmission system with NRZ-OOK modulation format and an in-line EDFA.

The output optical radiation of all 16 transmitters is combined into a single optical flow and sent through a 150 km long optical link, which consists of two sections (100 km and 50 km) of standard single-mode fibre (SMF) with 0.2 dB attenuation and 17 ps/nm/km chromatic dispersion at 1550 nm reference wavelength. The in-line EDFA is placed in between the two sections of the transmission line. After processing through the second SMF, the signal is sent through a fibre Bragg grating (FBG) for dispersion compensation purposes (total amount of compensated dispersion is 2550 ps/nm) and divided among 16 PIN photodiode based receivers with sensitivity of -20.5 dBm for $1 \cdot 10^{-9}$ reference bit-error ratio (BER).

Before choosing the configuration of the EDFA it is necessary to adjust the -3dB bandwidth of bandpass optical filters at the receiver end. For this purpose, the dependence of the maximal BER among all 16 channels (systems maximal BER) on the -3 dB bandwidth of optical filters is obtained at each channel spacing in a system without amplification and with transmission distance of 40 km. The obtained results are shown in Fig.2.

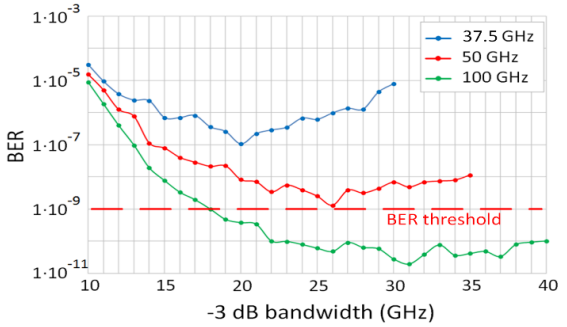

Fig. 2. Systems maximal BER value dependence on the -3 dB bandwidth of the optical filters for 35.7 (blue), 50 (red) and 100 GHz (green) channel spacing in the system without amplification.

As can be seen in Fig.2, in case when 100 GHz channel spacing, systems maximal BER value reaches its minimum ($1.96 \cdot 10^{-11}$, 13th channel) when the -3 dB bandwidth of optical filters is set to 31 GHz, in case of 50 GHz channel spacing – to 26 GHz ($2.98 \cdot 10^{-9}$, 8th channel), and in case of 37.5 GHz channel spacing – to 20 GHz ($1.07 \cdot 10^{-7}$, 4th channel). These results demonstrate that if the -3 dB bandwidth of optical filters is too small, part of the corresponding channel signal energy is filtered out, which causes severe signal quality degradation, and, on the contrary, if it is too big – part of the energy that belongs to the neighbouring channels is not filtered out and causes an increase of BER for the corresponding channel.

The in-line EDFA was based on a 12-meter long EDF, in which the 980 nm pumping radiation was propagating in the same direction as the amplified signal. The 980 nm wavelength was selected because, in general, at relatively high pump powers (30–100 mW) and relatively short spans of EDF, the 980 nm pump is capable of ensuring higher amplification efficiency than the 1480 nm pump, as due to the nonzero emission cross-section at 1480 nm the upper energy level is partially drained by the pump itself. Therefore, not all of the achieved population inversion is used to amplify the signal [6], [12], [13]. In order to find the lowest power of the 980 nm co-propagating pump that could ensure the required quality of the signal, the system maximal BER values were observed at different pump powers of the pump at 37.5, 50 and 100 GHz channel spacing. The obtained results are shown in Fig. 3.

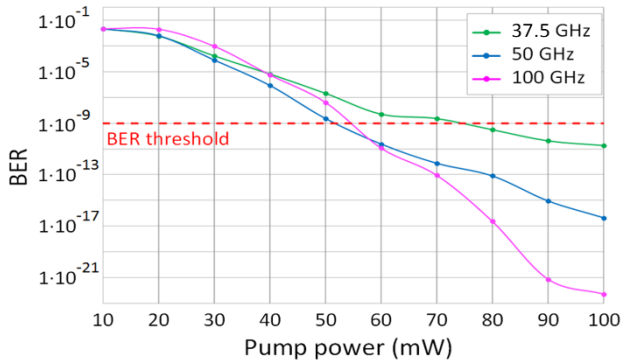

Fig. 3. Dependence of system maximal BER value on the power of the 980 nm co-propagating pump in the system with 37.5 (green), 50 (blue) and 100 GHz (pink) channel spacing.

The results displayed in Fig. 3 show that for 37.5 GHz channel spacing the minimal pump power that could ensure BER below the $1 \cdot 10^{-9}$ threshold was 80 mW. This is by 20 mW more than in the case of 50 GHz or 100 GHz channel spacing – in both cases only 60 mW were enough to ensure the required signal quality. The fact that the minimal pump power that ensured the required signal quality was the same in systems with 50 GHz and 100 GHz channel spacing indicated that for channel spacing of 50 GHz and higher the neighbouring channels caused inter-channel crosstalk that was too little to have a noticeable impact on the quality of the amplified signal.

It can also be seen that at lower pump powers in the system with 100 GHz channel spacing higher BER values were observed than in the systems with lower

channel spacing, but the situation changed with an increase in pump power. Such behaviour is caused by the EDFA gain spectrum slope – for 100 GHz channel spacing the wavelength band used for transmission was two times broader than for 50 GHz spacing. Due to the EDFA gain spectrum slope, in case of 100 GHz channel spacing channels with higher wavelength would obtain less amplification than in case of 50 GHz spacing; therefore, higher BER values were observed for these channels. At higher pump powers, the power of the channels becomes significant enough to induce arising of fibre non-linearity while being transmitted through the 2nd SMF. The less the channel spacing, the more explicit the arising of four-wave mixing (FWM), which results in higher amount of inter-channel crosstalk produced by channel-channel FWM (CC-FWM) . Therefore, when increasing the pump power for higher values of channel spacing, BER values are decreasing more rapidly than in systems with lower channel spacing. The chosen amplifier configurations ensured the following gain and noise figure (NF) values:

- System with 37.5 GHz channel spacing: the 80 mW 980 nm co-propagating pump ensured gain from 23.98 dB to 24.53 dB and NF from 4.47 to 4.5 dB.
- System with 50 GHz channel spacing: the 60 mW 980 nm co-propagating pump ensured gain from 22.38 dB to 23.33 dB and NF from 4.5 to 4.54 dB.
- System with 100 GHz channel spacing: the 60 mW 980 nm co-propagating pump ensured gain from 21.7 dB to 23.94 dB and NF from 4.48 to 4.56 dB.

These results show that in the case of the WDM system with 37.5 GHz spacing higher gain was required at approximately the same NF values to ensure BER below the $1 \cdot 10^{-9}$ threshold in comparison with systems with larger channel spacing. This can be explained by the fact that at 37.5 GHz channel spacing, to avoid inter-channel crosstalk from the neighbouring channels, the bandwidth of the optical filters needs to be so small, that it filters out a part of energy of the corresponding channel signal. This is why higher gain should be obtained to ensure the required signal power at the input of the photodetector. Such additional amplification was not required in the case of 50 GHz and 100 GHz channel spacing, as such spacing is high enough to avoid the previously described inter-channel crosstalk. Furthermore, as mentioned previously, inter-channel crosstalk produced by CC-FWM is more explicit in systems with lower channel spacing. Therefore, additional amplification was required in the system with 37.5 GHz channel spacing in order to compensate the signal impairments produced by CC-FWM.

To assess the EDFA performance, the dependences of BER values in the channels with the worst signal quality (in which BER values above the 10^{-9} threshold were detected first) on the power of the detected signal were obtained for all observed channel spacing values, and the results were compared with the same results obtained in WDM systems with the corresponding channel spacing but without amplification. The obtained results are shown in Fig. 4.

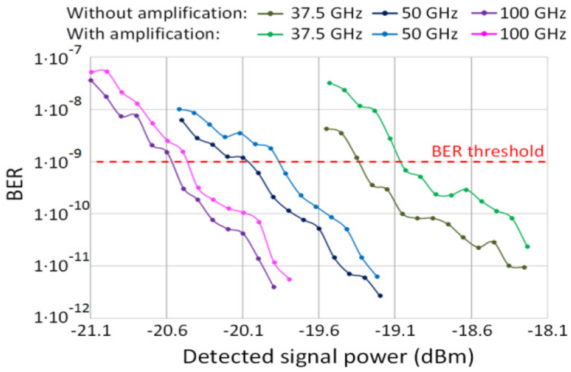

Fig. 4. Dependence of BER values in the channels with the worst signal quality on the power of the detected signal for three values of channel spacing in the WDM system with inline EDFA (37.5 GHz – green, 50 GHz – blue, 100 GHz – pink) and without amplification (37.5 GHz – olive, 50 GHz – dark blue, 100 GHz – violet).

Figure 4 shows that in the system with 100 GHz channel spacing implementation of the EDFA resulted in 0.1 dB power penalty in respect to the system without amplification, in the case of 50 GHz channel spacing – 0.18 dB, and in the case of 37.5 GHz channel spacing – 0.22 dB. It can be concluded that the smaller the channel spacing, the higher the power penalty. In all three cases, major part of power penalty is related to ASE noise produced by the EDFA. The NF values were approximately the same in all three cases; therefore, ASE produced by the EDFA was not the factor that caused the difference in power penalty. The cause of this difference was inter-channel crosstalk produced by fibre non-linearity. When the power of the signal is high enough, fibre nonlinearity arises during transmission, including CC-FWM and self-phase modulation (SPM) nonlinear effects. The efficiency of FWM increases with a decrease in the wavelength difference between the interacting spectral components. Therefore, the smaller the channel spacing, the higher the observed efficiency of FWM that occurs between the channels, and the higher amount of inter-channel crosstalk is produced. The presence of SPM also results in inter-channel crosstalk at relatively small values of channel spacing, as it causes broadening of the spectrum of the channels and results in overlapping of neighbouring channel spectra.

3. INVESTIGATION OF EDFA POSITIONING IMPACT ON THE QUALITY OF THE AMPLIFIED SIGNAL

From the perspective of amplifier positioning, amplifiers can be used in three different ways:

- As power boosters – the amplifier is placed at the output of the receiver block and is used to boost signal power right before sending it through the transmission fibre.
- As in-line amplifiers – the amplifier is placed in between two spans of transmission fibre and is used to compensate accumulated signal attenuation while the power of the signal is not too low for amplification or detection.

- As preamplifiers – the amplifier is placed at the input of the receiver block and is used to amplify the signal right before detection [6].

In this section, the authors investigate and compare the performance of the EDFA when it is used as a power booster, as an in-line amplifier or as a preamplifier. To reach this goal, a simulation model of a 9.953 Gbps WDM transmission system with NRZ-OOK modulation and total transmission distance of 100 km was introduced. Three different EDFA positioning scenarios were implemented – when the EDFA was used as a preamplifier (Fig. 5.A), as an in-line amplifier (Fig. 5.B) and as a preamplifier (Fig. 5.C).

The frequency region used for transmission in the simulation model shown in Fig. 5 was from 193 THz to 193.75 THz with 50 GHz channel spacing between the neighbouring channels – such setup was selected as per ITU-T G.694 grid for DWDM applications. The output radiation of all transmitters was combined and sent through a 100 km long transmission line that consisted of two 50 km long spans of standard SMF. When the EDFA was used as a power booster it was placed at the input of SMF1, when it was used as an in-line amplifier it was placed in between SMF1 and SMF2, and when it was used as a preamplifier – at the very input of the receiver block, after the FBG. EDF length and the parameters of the pumping radiation were selected in a way to obtain the minimal pump power that could ensure BER values below the 10^{-9} in all channels. Therefore, it was decided that the single-pump solution should be used in all three EDFA positioning scenarios. Same as in the previous section, it was decided to use the 980 nm co-propagating pump for obtaining population inversion in the EDF. Since in all three scenarios the power of the signal at the input of the EDFA was different, the length of the EDF was selected specifically for each EDFA positioning scenario.

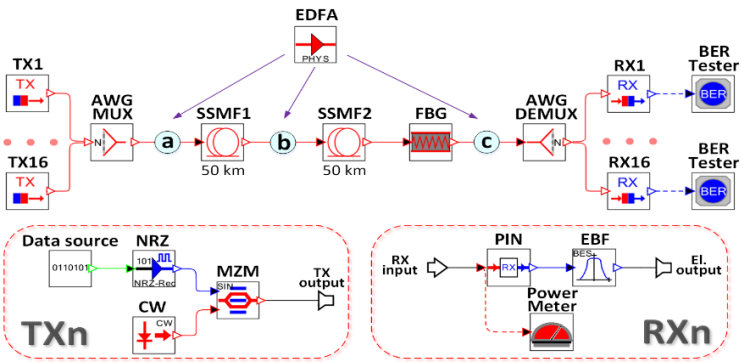

Fig. 5. Simulation model of the 16 channel 9.953 Gbit/s WDM transmission system with NRZ-OOK modulation and different EDFA positioning scenarios: (a) – as a power booster, (b) – as an in-line amplifier, (c) – as a preamplifier.

When choosing the configuration of the booster EDFA different combinations of EDF length and pump power were considered – the length of the EDF was changed from 5 metres to 15 metres and the dependence of systems maximal BER value on the power of the 980 nm co-propagating pump was obtained for each specific length of the EDF. Part of these results is shown in Fig. 6.A.

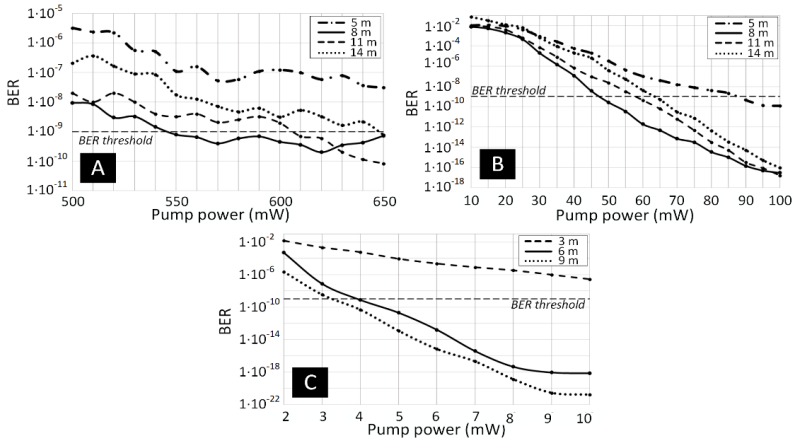

Fig. 6. Dependence of systems maximal BER value on the pump power of the booster (A) and the in-line (B) EDFA at EDF length of 5, 8, 11 and 14 metres, and of the preamplifier EDFA (C) at EDF length pf 3, 6, 9 metres.

Figure 6.A shows that the lowest pump power that ensured BER values below the $1 \cdot 10^{-9}$ threshold was 550 mW at EDF length of 8 metres ($7.92 \cdot 10^{-10}$ observed in the 15th channel). Based on these results, 550 mW 980 nm co-propagating pump and 8-metre long EDF was chosen for the system with the booster EDFA. The power of the signal at the input of the booster EDFA was 9.06 dBm. The on-off gain and NF of the EDFA with the above configuration varied from 12.74 dB to 12.94 dB and from 5.03 dB to 5.19 dB respectively among all 16 channels.

For EDF length below 8 metres the maximal achievable population inversion was not enough to ensure such level of amplification that could compensate the total optical loss in the system, because at such high input signal power the amplifier was operating in the saturation mode. The following tendency was observed – the longer the EDF, the higher the slope of the gain spectrum. Due to this slope of the provided on-off gain, some channels obtained less gain at a certain pump power than at a shorter EDF length; therefore, higher pump power was required to ensure a certain level of amplification for these channels. As a result, for EDF length greater than 8 metres a higher level of amplification could be achieved, but due to the slope of the gain spectrum higher pump power was required for the gain to be sufficient for all channels.

While configuring the in-line EDFA, the length of the EDF was changed from 5 to 15 metres and the power of the pump – from 10 to 100 mW for each specific length of the EDF. The obtained systems maximal BER value – pump power dependencies for EDF length of 5, 8, 11 and 14 metres are displayed in Fig. 6.B. As it is shown in Fig. 6.B, like in the case of the booster EDFA, the minimal pump power that could ensure the required quality of the signal was observed when an 8 metre-long EDF was used, but this pump power was 11 times lower than in case of the booster EDFA (BER $2.7 \cdot 10^{-10}$ observed in the 13th channel). Such EDFA configuration ensured from 12 dB to 12.88 dB on-off gain and from 5.12 dB to 5.3 dB NF values in the frequency region used for transmission.

Such significant difference between the system with the booster and the in-line EDFA in pump power required to ensure approximately the same level of

amplification could be explained by the difference of signal power at the input of these two amplifiers: input signal with higher power needed more population inversion to get the same gain in dB than an input signal with lower power, and to achieve such high population inversion higher pump power was required. In case of the in-line EDFA the power of the input signal was by 10.02 dB lower than in the booster EDFA (just -0.96 dBm). In case of the booster EDFA after amplification the power of the signal increased by 148.95 mW (from 8.05 mW to 156.5 mW), but in case of the in-line EDFA – by 12.83 mW (from 1.24 mW to 14.07 mW).

While configuring the preamplifier EDFA, the length of the EDF was increased from 3 to 9 metres and the power of the pump – from 2 to 10 mW for each specific length of the EDF. The obtained systems maximal BER value – pump power dependencies for EDF length of 3, 6 and 9 metres are displayed in Fig. 6.C. Figure 6.C shows that for the preamplifier EDFA just 4 mW of pump power at EDF length of 6 metres is enough to compensate the accumulated optical loss and to ensure BER values below $1 \cdot 10^{-9}$ ($7.59 \cdot 10^{-10}$ was observed in the 4th channel). Such amplifier configuration amplified the signal by 12.43–12.66 dB and ensured NF values from 5.26 to 5.48 dB in the frequency region used for transmission. The obtained results showed that for EDF length from 7 metres to 9 metres 4 mW was also enough to ensure the required quality of the signal, but at this point it was decided to use the shortest EDF. The total signal power at the input of the EDFA was just -13.94 mW, and after amplifying the signal by 12.43 – 12.66 dB its power increased just by 0.7152 mW (from 0.0404 mW to 0.7556 mW).

In order to determine the impact of EDFA positioning on the quality of the amplified signal, dependences of BER values on the power of the detected signal were observed in the channel with the worst signal quality (with the highest BER) in case of all three EDFA positioning scenarios, and these results were compared with the same results obtained in the corresponding channels of the same system without amplification. The obtained results in case of the booster EDFA are shown in Fig. 7(A), in case of the in-line EDFA – in Fig. 7(B) and in case of the preamplifier EDFA – in Fig. 7(C).

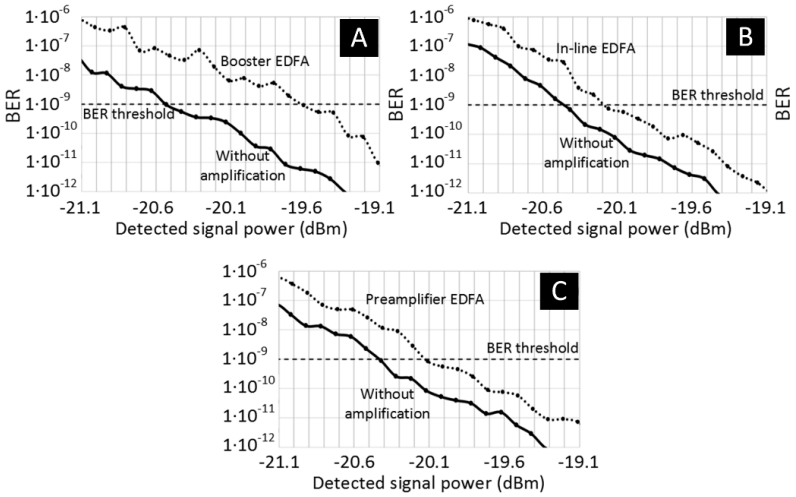

Fig. 7. Dependence of BER values on the power of the detected signal in the channels with the worst signal quality in the system without amplification (solid line) and with amplification (dotted line): (a) – power booster, (b) – in-line EDFA and (c) – preamplifier.

As can be seen from Fig. 7, when the EDFA was used as a power booster 0.92 dB of power penalty was observed in respect to the system without amplification, when it was used as an in-line amplifier – just 0.26 dB, and when it was used as a preamplifier – 0.31 dB. Part of this power penalty is caused by ASE noise. The remaining part of the power penalty in case of the power booster EDFA is related to inter-channel crosstalk produced by CC-FWM and SPM fibre non-linearity, which has arisen during transmission due to high power of the signal after amplification.

In cases when the EDFA was used as an in-line amplifier and a preamplifier, signal impairments produced by fibre non-linearity were not observed as the power of the signal at EDFA output was insufficient to cause any non-linear behaviour. The power penalty in respect to the system without amplification in case when the EDFA was used as a preamplifier was by 0.05 dB higher than in the case when the amplifier was placed in between the two spans of SMF. In the preamplifier scenario, the power of the signal at EDFA input was by 13 dB lower than in the in-line amplifier scenario and, therefore, could not use the obtained population inversion as efficiently as in the case of the in-line amplifier. As a result, the unused part of the achieved population inversion eventually resulted in producing additional ASE noise that caused the afore-mentioned additional 0.05 dB of power penalty.

4. CONCLUSIONS

While investigating the impact of changes in channel spacing on the desired EDFA configuration and its performance, the following conclusions have been made:

- Additional pumping may be required to ensure certain quality of the signal for channel spacing as low as 37.5 GHz to compensate the filtering out of part of the corresponding channel signal energy due to the presence of inter-channel crosstalk from the neighbouring channels.
- The dependence of the EDFA gain spectrum slope on the achieved level of population inversion and the impact of fibre non-linearity on the quality of the signal need to be considered while selecting the channel spacing in transmission systems with EDFAs. Due to the slope of the gain spectrum at lower pump powers in the system with 100 GHz channel spacing higher BER values have been observed than in systems with lower channel spacing. However, with an increase in pump power the situation becomes completely opposite as the gain spectrum becomes more even and as arising of fibre non-linearity becomes more explicit at lower values of channel spacing.
- If the power of the signal after amplification is significant enough to cause arising of fibre non-linearity then the smaller channel spacing is used, the higher the amount of inter-channel crosstalk produced by channel-channel FWM and the higher power penalty is observed in respect to a system without amplification. For 100 GHz channel spacing, this power penalty was equal to 0.1 dB, for 50 GHz channel spacing – 0.18 dB, and for 37.5 GHz channel spacing – 0.22 dB.

The following conclusions have been made while investigating the impact of EDFA positioning on the desired EDFA configuration and its performance:

- The higher the power of the signal at the input of the EDFA, the higher population inversion is required to ensure approximately the same level of amplification. To achieve a higher level of population inversion, higher pump power (and in some cases longer EDF) is required.
- At a certain point, decreasing signal power at amplifier input causes degradation of the quality of the amplified signal, as its power becomes insufficient to effectively consume the obtained population inversion. As a result, the unused population inversion causes an additional ASE noise that has negative impact on the amplified signal quality.

After summarising all of the previously mentioned results, it is evident that any change in the EDFA operating conditions (such as channel spacing or EDFA positioning) will impact the performance of the amplifier, and, therefore, after such changes the EDFA needs to be re-configured in order to use the amplifier as effectively as possible.

REFERENCES

1. Cisco Inc. (2018). *Cisco visual networking index: Forecast and trends*, 2017–2022. White paper.
2. Hamaide, J.P. (2015). *Optical networks: recent breakthroughs and future challenges.* France: Alcatel-Lucent Bell Labs CominLabs Days.
3. Morita, I., & Peng, W.R. (2012). High capacity WDM transmission using terabit super-channels. In *38th European Conference and Exhibition on Optical Communications*, 16–20 September 2012, Amsterdam, Netherlands, DOI:10.1364/ECEOC.2012.Th.2.C.3.
4. Digonnet, M. J. F. (2001). *Rare-earth-doped fiber lasers and amplifiers* (2nd ed.). USA: CRC Press.
5. Putrina, J., Olonkins, S., & Bobrovs, V. (2017). Investigation of amplification span length impact on the quality of the signal in WDM transmission systems with erbium-doped fiber amplifiers. In *2017 Progress in Electromagnetics Research Symposium (PIERS 2017)*, 22–25 May 2017, St. Petersburg, Russia. DOI:10.1109/PIERS.2017.8262033
6. Becker, P.C., Olsson, N.A., & Simpson, J.R. (1999). *Erbium-doped fiber amplifiers: Fundamentals and technology*. USA: Academic Press.
7. Putrina, J., & Bobrovs, V. (2016). Evaluation of erbium doped fiber amplifier application in fiber optics transmission systems. In *2016 Progress in Electromagnetics Research Symposium (PIERS 2016)*, 8–11 August 2016, Shanghai, China. DOI:10.1109/PIERS.2016.7735428
8. Sun, Y., Srivastava, A. K., Zhou, J., & Sulhoff, J.W. (1999). Optical fiber amplifiers for WDM optical networks. *Bell Labs Technical Journal*, *4*(1), 187–206.
9. Trifonovs, I., Bobrovs, V., & Ivanovs, G. (2011). Optimization of a standard bidirectional DWDM solution. *Electronics and Electrical Engineering*, *115*(9), 37–40.
10. Synopsys Inc. (2014). *Synopsys RSoft solutions*. Product Catalogue.
11. Ivanovs, G., Bobrovs, V., Olonkins, S., Alsevska, A., Gegere, L., & Parts, R. (2014). Application of the erbium-doped fiber amplifier in wavelength division multiplexing

(WDM) transmission systems. *International Journal of Physical Sciences*, *9*(5), 91–101.
12. Putrina, J. (2016). *EDFA characteristics and working principle evaluation in FOTS*. M.S. thesis. Riga: Riga Technical University.
13. Berezins, S., & Bobrovs, V. (2013). EDFA application research in WDM communication systems. *Electronics and Electrical Engineering*, *19*(2), 92–96.

EDFA PASTIPRINĀTĀJU DARBĪBAS IZPĒTE DAŽĀDOS EKSLPLUATĀCIJAS APSTĀKĻOS DWDM SAKARU SISTĒMĀS

J. Putrina, S. Olonkins, V. Bobrovs, J. Poriņš

K o p s a v i l k u m s

Šajā darbā ir izpētīta EDFA pastiprinātāju darbība atkarībā no tā ekspluatācijas apstākļiem. Pirmkārt, ir apskatīta starpkanālu intervāla izmaiņas ietekme uz pastiprināma signāla kvalitāti un uz optimālo EDFA konfigurāciju. Rezultāti tika iegūti pie trīs dažādiem starpkanālu intervāliem – 37.5 GHz, 50 GHz un 100 GHz. Otrkārt, tika novērtētā EDFA izvietojuma ietekme uz pastiprināmā signāla kvalitāti un uz optimālo EDFA konfigurāciju. Tika izskatīti trīs EDFA izvietojuma scenāriji – kad EDFA tika izmantots kā jaudas pastiprinātājs, kā līnijas pastiprinātājs un kā priekšpastiprinātājs. Visās apskatītās pārraides sistēmu konfigurācijās tika atrasta tāda EDFA pastiprinātāja konfigurācija kas spēja nodrošināt bitu-kļūdu attiecību zem $1 \cdot 10^{-9}$ vērtības visos pārraides sistēmas kanālos, izmantojot pēc iespējas zemāku pumpējošā starojuma jaudu. Pastiprinātāju darbības novērtēšanai pie katras izvēlētas EDFA konfigurācijas tika iegūtas nepieciešamās jaudas pieauguma vērtības attiecībā pret identisku pārraides sistēmu bez optiskā signāla pastiprināšanas.

18.02.2019.

sciendo

LATVIAN JOURNAL OF PHYSICS
AND TECHNICAL SCIENCES
2019, N 2

DOI: 10.2478/lpts-2019-0013

APPLIED PHYSICS

DEVELOPMENT OF PLANT FOR COATING AND DRYING OF LINSEED OIL

M. Gavars[1], J. Rudnevs[1], G.Tribis[1,2] M. Danieks[2]
[1] Riga Technical University, Faculty of Mechanical Engineering, Transport and Aeronautics, 36A Viskaļu Str., Riga, LV-1006, LATVIA
[2] EKJU Ltd., 12 Cecilu Str., Ieriki, Drabesi Village, Amata district, LV-4139, LATVIA
janis.rudnevs@rtu.lv

The aim of the research is to create a technological scheme for an industrial plant, which uses linseed oil (*Pone oleum*) paint as a finishing material upon working with coniferous wood components of different length and shape. On the basis of the technological scheme developed in the research, the prototype of the equipment will be produced at the factory of EKJU Ltd., with drying of products also being included.

***Keywords*:** *linseed oil, plant, prototype, wood*

1. INTRODUCTION

Due to a lack of industrial and commercial demand, one cannot purchase a ready-made linseed oil coating plant. Trends of ecological construction and increased consumption of paint of biological origin have brought this issue onto agenda and created a need for industrial equipment [1]. Moreover, various paints based on solvent have a negative impact on the surrounding environment that has contributed to regulatory efforts to limit the use of solvent in the future [2].

2. PROBLEM

Operations with linseed oil are considered craftwork, while in volumes the application of it could be done automatically. As mentioned earlier, due to relatively low demand there is no such plant, as well as various risk factors are existent. Caused by oxidation processes, rags smeared with linseed oil can heat and ignite. When self-ignition temperature is reached, the substance ignites in the presence of oxygen. Any oil in contact with clean oxygen may ignite or explode. When working with linseed oil, safety rules must be followed, and it is known that linseed oil, unlike water or

solvent base, is warming-up during the drying process. Due to a chemical process, it is prone to oxidation. This process can affect highly flammable products, such as paper, chips, but the flames cannot been observed immediately. The process takes time: the more the flammable material will have absorbed linseed oil, the sooner the flame may appear. However, the filter design of the plant may accumulate tiny particles of linseed oil, which through oxidation processes and in contact with dust may cause heating and self-igniting [3].

3. OBJECTIVE

The aim of the study has been to develop a technological scheme for a linseed oil (*Pone oleum*) application that could be used in industrial production as a finishing material for works with components of different length and shape and would dry them. The physicochemical properties of linseed oil are known, but deepened product research must be carried out, and subsequent technological solutions are necessary to make an industrially scalable linseed oil application plant that meets the needs of production. It is necessary to consider technological processes and conditions for development of a prototype of an experimental linseed oil application plant. The equipment must also be able to operate various units so that each of the units performs the task assigned to it. The possible prototype is displayed in Fig. 1 and marked with numbers: 1 – automatic loading with storage, 2 – exhaust and draining of chips and their dust, and various debris, 3 – heating of the surface of the component prior to dyeing, 4 – heating, re-circulation, and filtering of linseed oil; to achieve a high-quality coating, alignment of the material is performed during the application of linseed oil; removal of excess paint for re-use, 5 – discharge of preforms shall be performed after application of the paint. A cycle of re-application of linseed oil for the second or third rounds (layers) may be possible.

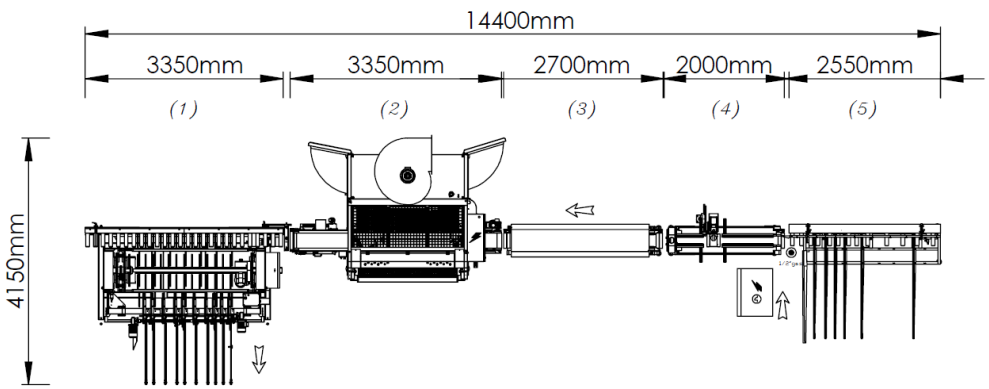

Fig. 1. Plant prototype.

4. DRYING PROCESS

In a natural environment, the process of drying of linseed oil may take up to several days until it is dry enough to stay intact upon direct contact with other surfaces, but the process of drying is continuing, and gradual hardening takes place [4]. EKJU ltd. conducted an accelerating experiment to speed up drying of linseed oil in order to be able to find a solution of what parameters must be present to accelerate the drying process to the utmost extent without losing the linseed properties simultaneously.

In an experiment, which tested the effects of temperature on paint drying, parameters characterising the process typically – adhesion and soakiness – were assessed. Planed pine (*pinus*) samples with a humidity of wood of 18 % (85x250 mm) were treated at a temperature of 25 °C or 40 °C after coating and the degree of drying was checked after certain periods of time. The paint-coated surfaces were no longer sticky after a 20-minute drying, but the spirit stain-coated surfaces reached such a state one hour later. When comparing the coatings to each other, the samples dried under a temperature of 40 °C were no longer soaked after 2 hours, while those of spirit stain reached this condition after 24 hours. It took more than 24 hours to reach a condition where both painted and spirit stain-coated surfaces were no longer soaked. These results show that increased temperatures affect drying of the first layer. The effect of temperature on the second layer, regardless of the temperature after 24 hours, resulted as follows: although the coating no longer soaked, it dipped by squeezing. In the case of use of paint and spirit-stain, drying at high temperatures is not effective enough to ensure rapid drying of the second layer.

An ultraviolet (UV) radiation experiment was conducted for acceleration of drying to test the effects of UV radiation on drying of coating. A UV-blacklight lamp with a capacity of 13W was used, radiation was 315 to 400 nm in the area, and radiation intensity on the surface of samples was 700μW/cm^2. Samples were irradiated for 4 hours, but none of the coatings were dried completely during that time. The stage of drying was tested by rubbing the surface with a cotton slab and by visual assessment of the presence or absence of coating pigments on the slab.

According to the data obtained in the study, it is possible to evaluate the provision of an artificial drying process in the plant unit.

5. HEATING OF LINSEED OIL

A similar experiment was conducted with heating of linseed oil. Three coatings were used in the study: black linseed oil colour, white linseed spirit stain, and grey linseed water emulsion. The viscosity for all coatings was determined at three temperatures: 25 °C, 35 °C, 45 °C, ensuring a stable (± 0.5 °C) solution temperature throughout the effluence period. The coating densities and effluence periods with viscosity-determination are given in Table 1.

Of the coatings studied, the lowest temperature impact on viscosity is for emulsions which, when the temperature is increased by 20 °C, will reduce the effluence period by 24 % while the paint and spirit stain have a reduction of 33 % to 34 %. After the coating was dried, samples were sawn, and microscopy

samples were prepared for each sample taken from at least 10 points. The results of microscopy show that although viscosity of the emulsion at 40 °C is lower, it does not significantly affect depth of its penetration in the wood by spraying the coating and, in both temperatures, penetration is no more than 2–3 cell layers on average.

Table 1

Densities and Effluence with Viscosity-Determination, Depending on Temperature
** diameter of viscosimeter aperture – 4 mm; ** diameter of viscosimeter aperture – 2 mm*

	Paint*	Spirit stain*	Emulsion**
Viscosity			
Temperature, °C	Effluence period, s		
25	187	45	217
35	149	36	190
45	124	30	166
Density, g/cm^3			
	1.30	1.11	0.98

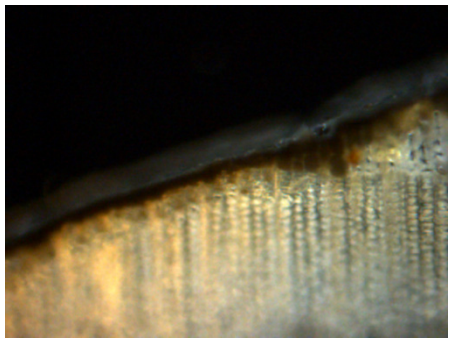

Fig.2. Microscopy image of the cross-section of sample sprayed with linseed oil at 30 °C (100 x magnification).

6. TECHNICAL SOLUTION TO THE PLANT

The plant feed speed shall be set from 15 m/min to 30 m/min. The preforms for painting will be loaded automatically from the stocking table with a minimum of 15 components, and the components will be wiped, and chips and dust of chips will be sucked out. Preforms shall be pre-heated from 35 °C to 40 °C before the finishing material is released. This finishing material will be applied to components at a temperature of 35 °C to 45 °C, maintaining a withheld viscosity. The application of the finishing material is designed from 3 to 5 sides, the layer being of thickness of 40 g/m^2. The extra linseed oil will be removed from the conveyor belt mechanically with a scraper and used for re-application to subsequent parts, the paint will be filtered. The application zone requires additional attention, taking into account the various risk factors for oxidation of linseed oil and requiring ventilation with an air exchange of 10,000 m^3/h with a changeable filter. A storage unit of freshly painted preforms is designed for drying of preforms within a period of 40 to 60 minutes, followed by brushing/sweeping of preforms with specially selected brushes. This unit is intended

to be individually connected and detachable from the total equipment, so that the components can, if necessary, be directed to drying without brushing/sweeping, bringing the components to the discharge unit. The drying unit is not incorporated into the plant directly, but for the purpose of the overall technological process, the coated parts will be delivered to a specially equipped drying room (chamber) with the possibility to transfer the dried parts to the re-application cycle of the finishing material in the dyeing plant or delivered to the re-brushing/sweeping in the plant assembly.

The plant will ensure that the following settings are met: no more than 5 to 10 litres of paint are needed to replace the colour tone during the washing of the plant by the end of the finishing process or shift. The control panel of the plant will be placed in a free-standing cabinet, and it will include all switches, safety systems and indicating lamps. The control cabinet will be equipped with ventilation and full dust protection, and the plant will be equipped with perimeter protection.

7. CONCLUSION

The technical solution provided for the plant does not cover drying unit, as the drying process has not been accelerated in an artificial manner during the experiment significantly, or it has not been effective to a large extent. This is the reason why a separate room (drying chamber) may be offered to store the components coated with the finishing material in order to ensure that drying is provided under controlled conditions and is slightly accelerated.

An in-depth study of the amount of finishing material is needed to mitigate the loss of linseed oil by wiping. A more accurate amount of linseed oil needed for paint and spirit stain to avoid wiping can be calculated.

A few unique solutions have been presented to the plant, mainly in terms of safety, as attention should be paid to oxidation processes of linseed oil, which may cause its self-ignition. Solutions have been found to improve the quality of work and the previously manual application of linseed oil could be automated.

Particular emphasis must be paid to cleaning of the plant because under no circumstances linseed particles can be accumulated in the units (nodes) of the plant and its ventilation system. The plant and its ventilation system will be equipped with special smoke and heat detectors which, if needed, will send an emergency signal to the console of the plant and stop the equipment, as well as the emergency signal will be sent to the plant fire control centre and will trigger the alarm to eliminate emergency conditions. Location of the painting equipment shall be determined in a separate building to mitigate risks of fire and prevent threats other nearby buildings could be potentially exposed to.

ACKNOWLEDGMENTS

The authors gratefully acknowledge the Forest Sector Competence Centre of Latvia for the financial support of the research, in the framework of the project No. 1.2.1.1/16/A/009

REFERENCES

1. Olsson, A. M., & Sandberg, D. (1996). Analysis of the interaction between wood and high solid linseed oil paint. *Modern Adhesion Theory Applied on Coating and Gluing of Wood,* 1–13.
2. Chang, C. W., Chang, J. P., & Lu, K. T. (2018). Synthesis of linseed oil-based waterborne urethane oil wood coatings. *Polymers, 10*(11), 1235.
3. Dlugogorski, J. B. Z., Kennedy, E. M., & Mackie, J. C. (2012). Low temperature oxidation of linseed oil. *Fire Science Reviews*, *1*(1), 1–36.
4. Lazzari, M., & Chiantore, O. (1999). Drying and oxidative degradation of linseed oil. *Polymer degradation and stability, 65*(1), 303–313.

LINEĻĻAS KRĀSAS UZKLĀŠANAS UN ŽĀVĒŠANAS IEKĀRTAS TEHNOLOĢISKO SHĒMU UN RASĒJUMU SAGATAVOŠANA

M. Gavars, J. Rudņevs, G.Tribis M. Danieks

K o p s a v i l k u m s

Šī darba mērķis bija pētniecības projekta Nr.1.2.1.1/16/A/009 ietvaros radīt tādas rūpnieciski izmantojamas iekārtas tehnoloģisko shēmu, kura kā apdares materiālu izmanto lineļļas (*Pone oleum*) krāsu vai beici, darbā ar dažādām garuma un formas koka detaļām, ietverot produktu nožāvēšanu. Ir zināmas lineļļas fizikāli ķīmiskās īpašības, bet, lai izgatavotu ražošanas vajadzībām atbilstošu rūpnieciski mērogojamu lineļļas uzklāšanas iekārtu, bija nepieciešama padziļināta produktu un procesu izpēte un tai sekojošu tehnoloģisko risinājumu izstrāde. Pēc padziļinātas lineļļas krāsas un beices īpašību izpētes tika radīta iespējamā prototipa skice.

Izskatot tirgū pieejamo krāsu uzklāšanas iekārtu piedāvājumu, tika secināts, ka gatavu lineļļas krāsas uzklāšanas iekārtu nav iespējams iegādāties, sekojošu iemeslu dēļ:

1. Šādai iekārtai nav rūpnieciska un komerciāla pieprasījuma;
2. Pastāv dažādi riska faktori, piemēram, ar lineļļu sasmērētas lupatas oksidējoties, var sakarst un aizdegties. Kad sasniegta pašaizdegšanās temperatūra, viela skābekļa klātbūtnē uzliesmo. Jebkura eļļa, kontaktējoties ar tīru skābekli, var aizdegties vai uzsprāgt. Strādājot ar lineļļu, jāievēro drošības noteikumi, ir zināms, ka lineļļa žūšanas procesā uzsilst, atšķirībā no ūdens vai šķīdinātāja bāzes krāsas. Tā vietā ķīmiska procesa dēļ tā ir pakļauta oksidācijai.

Izstrādājot lineļļas iekārtas uzklāšanas mezglu tehnisko risinājumu, tika ņemti vērā lineļļas uzklāšanas eksperimenti uzsildot krāsu un beici, lai iegūtu labāko viskozitāti. Mikroskopijas rezultāti parādīja, ka, lai arī emulsijas viskozitāte pie 40°C ir zemāka nekā pie 25°C, tas būtiski neietekmē tās iespiešanās dziļumu koksnē,

pārklājumu uzklājot ar uzsmidzināšanas paņēmienu, un abu temperatūru gadījumā iespiešanās vidēji nav dziļāka par 2 – 3 šūnu slāņiem.

Saskaņā ar projekta rūpnieciskā pētījuma dotajām vērtībām tika atrasts ražotājam piemērotākais tehniskais risinājums iekārtas tehnoloģisko shēmu rasējuma izstrādei, kurā tika iestrādātas tādas iespējas kā krāsojamo sagatavju automātiska ielāde un izlāde no uzkrājuma galda, pirms uzklāšanas sagatavju virsmu uzsilde no 35 līdz 40°C. Apdares materiāla uzklāšanas veids paredzēts no 3-5 pusēm, plānā kārtā 40gr/m^2.

Pētniecības projekta ietvaros tika veikti arī paraugu žāvēšanas eksperimenti, lai izpētītu, pie kādiem parametriem lineļļa visātrāk nožūst, nezaudējot savas īpašības, kas ir ļoti būtiski produktu ražotājam. Žāvēšanas paātrināšanai tika veikts eksperiments arī ar ultravioleto starojumu (UV), lai pārbaudītu UV starojuma ietekmi uz pārklājuma žūšanu

Žāvēšanas mezgls netiek tieši iekļauts iekārtā, taču, kopējā tehnoloģiskā procesa nodrošināšanai, pārklātās detaļas tiks nogādātas speciāli aprīkotā žāvēšanas telpā (kamerā) ar iespēju nožuvušās detaļas pārvietot uz atkārtotu apdares materiāla uzklāšanas ciklu krāsošanas iekārtā vai nogādātas uz atkārtotu nobirstēšanu/ noslaucīšanu iekārtas mezglā. Vadības skapis tiks aprīkots ar ventilāciju un pilnīgu putekļu aizsardzību, kā arī iekārtai tiks uzstādīta perimetra aizsardzība.

04.02.2019.

sciendo

LATVIAN JOURNAL OF PHYSICS
AND TECHNICAL SCIENCES
2019, N 2

DOI: 10.2478/lpts-2019-0014

SOLID STATE PHYSICS

MAGNON AND PHONON EXCITATIONS IN NANOSIZED NiO

N. Mironova-Ulmane [1], A. Kuzmin [1], I. Sildos [2], L. Puust [2], J. Grabis [3]
[1] Institute of Solid State Physics, University of Latvia,
8 Kengaraga Str., Riga, LV-1063, LATVIA
E-mail: nina@cfi.lu.lv
[2] Institute of Physics, University of Tartu, 1 Ostwaldi, 50411 Tartu, ESTONIA
[3] Riga Technical University, Institute of Inorganic Chemistry,
3/7 P. Valdena Str., LV-1048, Riga, LATVIA

Single-crystal, microcrystalline and nanocrystalline nickel oxides (NiO) have been studied by Raman spectroscopy. A new band at ~200 cm^{-1} and TO-LO splitting of the band at 350–650 cm^{-1} have been found in the spectra of single-crystals NiO(100), NiO(110) and NiO(111). The Raman spectra of microcrystalline (1500 nm) and nanocrystalline (13–100 nm) NiO resemble those of the single crystals. They all contain the two-magnon band at 1500 cm^{-1}, indicating that the oxides remain at room temperature in the antiferromagnetic phase. Besides, a new sharp Raman band has been observed at 500 cm^{-1} in nanocrystalline NiO. Its temperature dependence suggests the magnetic origin of the band, possibly associated with the one-phonon–one-magnon excitation at the Brillouin zone centre.

Keywords*: lattice dynamics, magnons, nickel oxide, nanoparticles, Raman spectroscopy*

1. INTRODUCTION

Nickel oxide (NiO) is a versatile compound, which finds numerous applications in rechargeable batteries [1], smart windows [2], catalysis [3], sensors [4], gamma radiation detectors [5], resistive memories [6] and magnetoresistive devices [7].

Bulk NiO is a highly correlated material, which features a Mott insulating character and a type-II easy-plane antiferromagnetic (AFM) ordering. Therefore, the understanding of its electronic structure and bonding was a challenging theoretical task for decades. In the paramagnetic phase above the Néel temperature T_N = 523 K, NiO has a centrosymmetric cubic rock-salt crystal structure (space group No. 225, *Fm-3m*) with nickel ions located at the centres of regular NiO_6 octahedra [8]. The ferromagnetic ordering of spins of Ni^{2+} ions occurs below T_N in {111} sheets, with adjacent sheets having antiparallel spins [9], [10]. Such spin ordering leads

to a magnetostriction effect, causing a week cubic-to-rhombohedral distortion (space group No. 166, *R-3m*) of the NiO structure [8], [11]–[15], The distortion is accompanied by splitting (about 10–40 cm^{-1} at 300 K) of the zone centre transverse optical (TO) mode [16]–[18]. The magnetic structure of NiO nanoparticles differs from that of the bulk because of the finite-size effects and the presence of defects [19]. A complex magnetic structure composed of as many as up to eight-sublattice spin configurations was proposed for NiO nanoparticles [20]–[22] in contrast to the single-crystal NiO, having the two-sublattice magnetic structure [8]. Apart from the antiferromagnetically ordered core, magnetically-disordered uncompensated spins exist at the surface of NiO nanoparticles [23]–[29], leading to a super-paramagnetic behaviour [30].

Neutron diffraction studies of plate-shaped NiO nanoparticles with a thickness of ~2 nm indicated a reduction of the Néel temperature by ~60 K [31]. Comparison of X-ray and neutron diffraction data also evidenced the identity of the magnetic and crystallographic correlation lengths, suggesting that each NiO nanoparticle consists of a single magnetic domain [31]. Finally, a significant lattice expansion and a crossover in magnetic properties occur in NiO nanoparticles when their size decreases below 30 nm [32]. An increase of the lattice parameter in NiO nanoparticles upon a decrease of their sizes was observed below 20 nm in [33] and below 12 nm in [34].

The magnetic ordering and lattice dynamics of microcrystalline and single-crystalline NiO were studied by Raman spectroscopy in [35]–[42]. The Raman spectrum of bulk NiO at room temperature consists of several bands due to second-order phonon scattering (2TO band at ~730 cm^{-1}, TO+LO band at ~906 cm^{-1} and 2LO band at ~1090 cm^{-1}) and two-magnon band (at ~1500 cm^{-1}) [35]–[38], [40], [42]. The main difference between green (stoichiometric) and black (defect-reach) bulk NiO was a dramatic increase in the strength of the one-phonon LO mode at 550-560 cm^{-1} in the black NiO [35]. The origin of phonon bands was interpreted theoretically using the rigid-ion [43]–[46], shell [47], and first principles [42], [48] models. It was also proposed that some nonmagnetic properties of NiO as zone-centre optical phonon frequencies and Born effective charge tensor are substantially noncubic below the Néel temperature, even assuming the ideal rock-salt structure of the oxide [49].

The influence of finite-size and preparation conditions on the vibrational properties and magnetic ordering in nanocrystaline NiO was studied by Raman spectroscopy in [28], [34], [50]–[54]. The phonon-related bands in the Raman spectra of large green nanocrystals (100–1500 nm), produced by radio-frequency plasma technique, are close to those in the bulk [50]. However, the enhancement of the band at 500 cm^{-1} was found in small black nanocrystals (13–23 nm) produced by precipitation method, and the band was associated with the phonon-magnon coupling at the nanoparticle surface or with the presence of defects [51].

Small NiO nanoparticles (3.5–12.4 nm) were produced in [34] by a decomposition of nickel acetate at different temperatures. Their Raman spectra resemble those in [50]. Still, they do not show any peak related to the magnon excitation at 1500 cm^{-1} as well as any enhancement of 500 cm^{-1} band [34]. A contribution from surface modes to the broadening of LO and 2LO bands was also

proposed in [34].

The sol-gel method followed by annealing in air was employed in [52] to synthesize NiO nanoparticles in the range of 16.6–54 nm. The Raman spectrum of the smallest particles (16.6 nm) was dominated by the one-phonon (TO and LO) scattering; however, the two-phonon and two-magnon bands became also visible upon increasing particle size. Close results were obtained for nanosized NiO powders prepared by ball milling process under different milling speeds in [53]. In the latter case, a decrease of the crystallite size from 43 nm to 10.5 nm led to a reduction of the two-phonon band intensity, whereas the two-magnon band was not detected in all milled samples [53].

Nanocrystalline NiO (~26–36 nm) with filamentary morphology and large amount of nickel vacancies was produced by the template-based method using the cellulose template [54]. As a result, the one-phonon Raman bands (TO at 400 cm^{-1} and LO at 500 cm^{-1}) were strongly enhanced compared with the two-phonon band at ~1090 cm^{-1}. In addition, the presence of the intense two-magnon band at ~1500 cm^{-1} indicated the existence of the antiferromagnetic order at room temperature. Note that similar Raman spectra were observed for NiO nanoparticles in the range of 6.1–79.8 nm prepared by the precipitation method [28], except that the two-magnon peak disappeared for the 6.1 nm sample.

In the present study, we have employed the temperature-dependent Raman spectroscopy to probe the phonon and magnon dynamics in single-crystal NiO with different orientations (100), (110), (111) and in NiO nanoparticles. Two new bands at ~200 cm^{-1} and ~500 cm^{-1} have been evidenced, and their origin will be discussed.

2. EXPERIMENTAL STUDY

Nanocrystalline NiO powders were produced by two methods. A precipitation method, based on a reaction of aqueous solutions of $Ni(NO_3)_2 \cdot 6H_2O$ and NaOH with subsequent annealing in air at several temperatures up to T_{an} = 450 °C, was employed to produce the smallest black NiO nanoparticles. Their average sizes were estimated from the BET specific surface area measurements and were equal to about 13 nm for powders annealed at T_{an} = 250 °C and 300 °C, 17 nm at T_{an} = 350 °C, and 23 nm at T_{an} = 450 °C. In the second method, green NiO particles with larger size of 100 nm and 1500 nm were prepared by evaporation of coarse grained commercially available NiO (99.9 %) powder with the particle size in the range of 20–40 μm in the radio-frequency plasma [50].

Three green coloured single-crystals NiO(100), NiO(110) and NiO(111) were grown on top of MgO(100), MgO(110) and MgO(111) single-crystal substrates, respectively, using the method of chemical transport reaction [55], [56].

The Raman spectra were measured with large signal/noise ratio and particular attention to exclude any unintentional sample overheating by the laser light. High-temperature (20–290 °C) Raman experiments were conducted using a confocal microscope with spectrometer Nanofinder-S (SOLAR-TII, Ltd.). The measurements were performed through 20× optical objective. The Raman spectra were excited by a solid-state DPSS 532 nm laser (max cw power 150 mW). The Peltier-cooled back-

thinned CCD camera was used as a detector. The elastic laser light component was eliminated by the edge filter (Semrock RazorEdge, LP03-532RE-25). The sample temperature was controlled by self-made optical furnace. Room temperature Raman spectra were also measured through 50× microscope objective using Renishaw inVia micro-Raman spectrometer equipped with argon laser (514.5 nm, max cw power 10 mW). The spectral signal was dispersed by the 2400 grooves/mm grating onto Peltier-cooled (-60 °C) CCD detector.

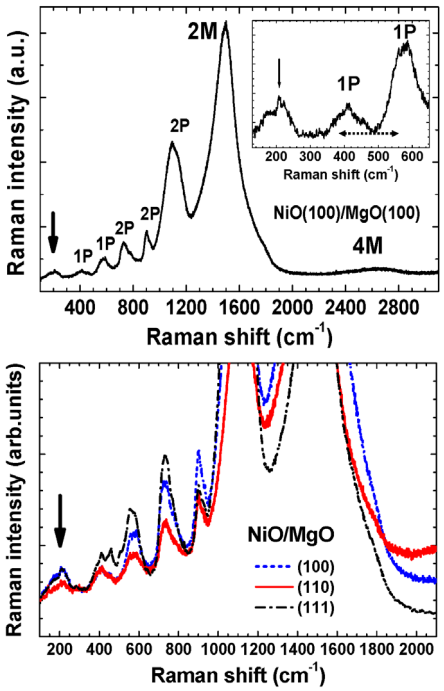

Fig. 1. Room temperature Raman spectra of green single-crystals NiO(100), NiO(110) and NiO(111). Enlarged low-frequency range is shown in the inset. The arrows indicate previously unclassified band at ~200 cm^{-1}.

3. RESULTS AND DISCUSSION

Room temperature Raman spectrum of single-crystal NiO(100) consists of several bands above 300 cm^{-1} (Fig. 1). According to the previous assignment in [35], [36] based on the cubic NiO structure, the first five bands are due to the phonon scattering: one-phonon (1P) TO and LO modes (at ~400 cm^{-1} and ~580 cm^{-1}, respectively), two-phonon (2P) 2TO modes (at ~730 cm^{-1}), TO+LO (at ~906 cm^{-1}) and 2LO (at ~1090 cm^{-1}) modes. The strongest band at 1500 cm^{-1} is due to the two-magnon (2M) scattering [35], [37]. Note that the band at ~2640 cm^{-1} corresponds to the four-magnon (4M) scattering [36]. At 1.5 K, the 4M band is located at ~2800 cm^{-1} and has a pronounced shape [36], but it broadens and shifts to lower frequencies as temperature increases. Two differences are observed between the Raman spectra of single-crystals NiO in Fig. 1 and those measured in [35], [38], [40]: the one-phonon band at ~350–650 cm^{-1} is split into two (TO and LO) bands located at ~400 and ~580 cm^{-1}, and a new band appears at ~200 cm^{-1}. Note that the TO-LO splitting

of the one-phonon band has also been observed in the recent study [42]. We attribute the origin of the band at 200 cm^{-1} to the zone-boundary phonon mode [57].

Temperature dependence of the Raman spectra for two stoichiometric single-crystals NiO(100) and NiO(111) is shown in Fig. 2. The main visible effect is related to a decrease of intensity and a displacement to lower frequencies of the two-magnon band at ~1500 cm^{-1}, when the sample temperature is approaching the Néel temperature. The band at 200 cm^{-1} as well as the two (TO and LO) bands at 400 and 580 cm^{-1} remain well visible at all temperatures. One can also see that the TO band at 400 cm^{-1} exhibits splitting below the Néel temperature due to the magnetic-order induced phonon anisotropy [16], [18], which appears at room temperature as a shoulder or a narrow peak located at 460 cm^{-1} in the Raman spectrum of single-crystal NiO(111).

Room temperature Raman spectra of nanocrystalline (13–23 nm) NiO (Fig. 3), produced at different annealing temperatures in the range of 250–450 °C, are rather similar to that of the bulk material except for a narrow strong band around 500 cm^{-1}. The phonon-related Raman bands (1P and 2P in Fig. 3) in nanocrystalline NiO are close to those in single-crystals: they consist of a small band (1P) at ~200 cm^{-1}, a wide one-phonon (1P) band at ~300-600 cm^{-1} and two-phonon (2P) bands at ~730 cm^{-1}, ~900 cm^{-1} and ~1100 cm^{-1}. The intensity of the one-phonon (1P) bands relative to that of the 2P bands is higher in nanopowders due to the presence of defects or surface effect, while the three two-phonon (2P) bands appear to be more broadened than in single-crystal NiO. Similar behaviour of the phonon-related Raman bands in nanopowders was reported in [58]. The two-magnon (2M) band located at ~1500 cm^{-1} has in nanopowders smaller intensity compared to the two-phonon band at ~1100 cm^{-1} since the size effect limits the long-range magnetic order.

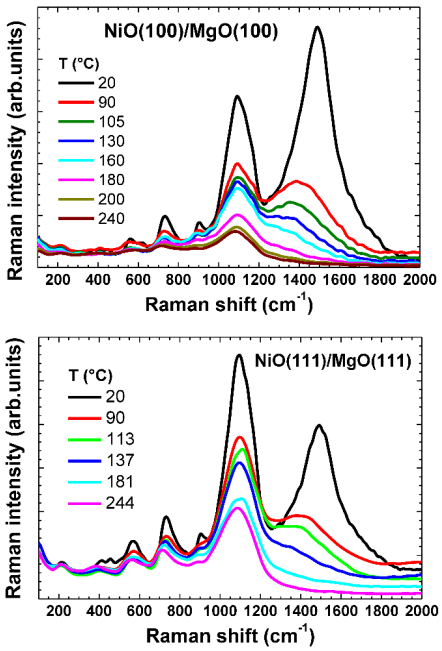

Fig. 2. Temperature dependent Raman spectra of green single-crystals NiO(100)/MgO(100) and NiO(111)/MgO(111) measured in the temperature range between 20 °C and 250 °C.

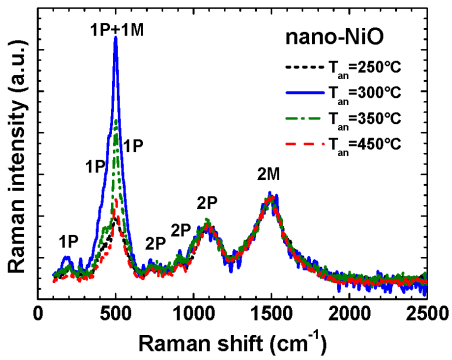

Fig. 3. Room temperature Raman spectra of nanocrystalline (13–23 nm) NiO powders produced by annealing at different temperatures. Laser excitation power P_{ex} = 0.1 mW.

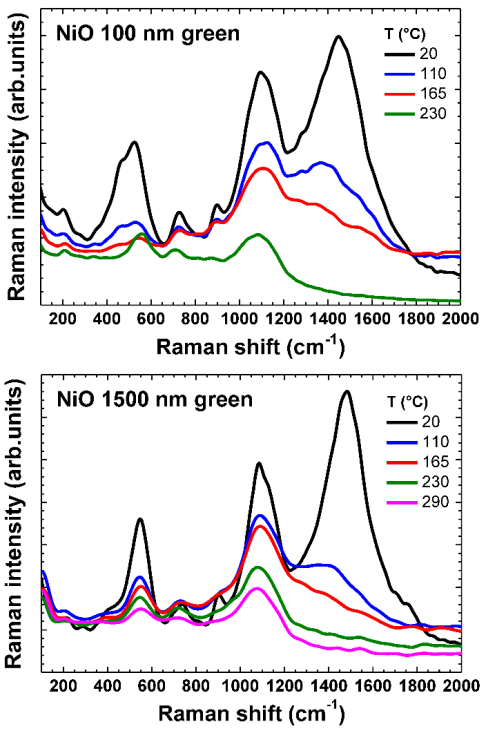

Fig. 4. Temperature dependent Raman spectra of nanocrystalline (100 nm) and microcrystalline (1500 nm) NiO powders.

Temperature dependence of the Raman scattering in nanocrystalline (100 nm) and microcrystalline (1500 nm) NiO powders is shown in Fig. 4 and is close to that in single-crystal NiO in Fig. 2. The most intriguing fact is the behaviour of the band at ~400–600 cm^{-1}. Its intensity at room temperature is rather high and correlates with the intensity of the two-magnon band at 1500 cm^{-1}, which decreases upon heating until it disappears approaching the Néel temperature. Therefore, one can suspect that the band at ~400–600 cm^{-1} has some magnon-related origin.

Heating of the sample can be achieved not only in an optical furnace, but

also when the laser power is changed. In this case, the precise value of temperature is not known but for NiO can be roughly estimated from the intensity and position of the two-magnon band at ~1500 cm^{-1}. Such an experiment was conducted for nanocrystalline (17 nm) NiO powder. The obtained Raman spectra are shown in Fig. 5. We started at the low laser power of P_{ex} = 0.1 mW at the sample with no sample heating as is evidenced from the large intensity of the two-magnon band. Upon increasing the laser power ten times up to P_{ex} = 1 mW at the sample, the intensity of the two-magnon band decreases, and its position shifts down to ~1400 cm^{-1}. The shift of the two-magnon band contributes to a change in the background under other bands, thus making problematic their proper normalization [42]. At the same time, the position of the phonon-related bands remains nearly unchanged upon laser heating. Further increase of the laser power to P_{ex} = 5 mW at the sample leads to a complete disappearance of the two-magnon band, suggesting heating above the Néel temperature and, thus, destruction of the magnetic ordering. Note that when the laser power is decreased back to P_{ex} = 0.1 mW, the shape of the Raman spectrum is completely restored to the original one, indicating the reversibility of the transition and the absence of any sample damage.

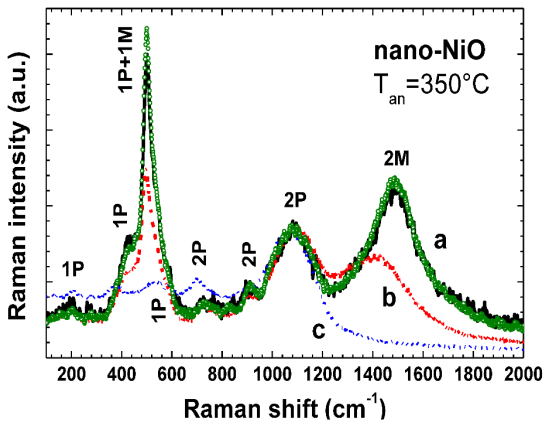

Fig. 5. The Raman spectra of nanocrystalline (17 nm) NiO powder (annealed at 350 °C) measured at different laser excitation powers: (a) P_{ex} = 0.1 mW (solid line – the first measurement; open circles – the final measurement); (b) P_{ex} = 1 mW; (c) P_{ex} = 5 mW. The phonon and magnon related bands are indicated.

Note that the Raman spectrum of nanocrystalline (17 nm) NiO powder contains a narrow band at 500 cm^{-1}, which is temperature dependent and correlates well with the two-magnon band (Fig. 5). This band also demonstrates the dependence on the size of nanocrystallites in Fig. 3. Therefore, we tentatively attribute the origin of this band to scattering by two particles: one-phonon (~440 cm^{-1}) and one-magnon (~40 cm^{-1}) excited simultaneously at the Brillouin zone centre due to the strong phonon-magnon coupling occurring at the nanoparticle surface or defects. Upon a decrease in the nanoparticle size, the intensity of the band at 500 cm^{-1} changes as a result of the competition between two processes: (i) an increase in the surface-to-bulk ratio and defect concentration, and (ii) a destruction of the long-range magnetic ordering [59].

4. CONCLUSIONS

Raman scattering by phonons and magnons has been studied in single-crystal, microcrystalline (1500 nm) and nanocrystalline (13–100 nm) NiO powders. The Raman spectra of nanocrystalline NiO have been found to be qualitatively similar to those of single-crystal, including the two-magnon band at 1500 cm^{-1}, indicating that the nanopowders remain at room temperature in antiferromagnetic phase.

A weak but clearly visible new band at ~200 cm^{-1} has been found in the Raman spectra of all samples and attributed to the zone-boundary phonon mode [57]. TO-LO splitting of the phonon band at 350–650 cm^{-1} has been observed in single-crystal NiO. Moreover, the TO band at 400 cm^{-1} is split below the Néel temperature due to the magnetic-ordering induced phonon anisotropy [16], [18]. This effect appears at room temperature as a shoulder or a narrow peak located at 460 cm^{-1} in the Raman spectrum of single-crystal NiO(111). Finally, a sharp intense Raman band has been observed at 500 cm^{-1} in smallest (~13–17 nm) black nanocrystalline NiO powders. The band is located on top of one-phonon bands, and its temperature dependence correlates with that of the two-magnon band at 1500 cm^{-1}, thus suggesting the magnetic origin of the band, possibly associated with the one-phonon–one-magnon excitation at the Brillouin zone centre. The traces of this band have also been detected in microcrystalline NiO powder.

REFERENCES

1. Lee, D. U., Fu, J., Park, M. G., Liu, H., Ghorbani Kashkooli, A., & Chen, Z. (2016). Self-assembled NiO/$Ni(OH)_2$ nanoflakes as active material for high-power and high-energy hybrid rechargeable battery. *Nano Lett.*, *16*, 1794–1802. DOI: 10.1021/acs.nanolett.5b04788
2. Browne, M., Nolan, H., Berner, N., Duesberg, G., Colavita, P., & Lyons, M. (2016). Electrochromic nickel oxide films for smart window applications. *Int. J. Electrochem. Sci.*, *11*, 6636–6647. DOI: 10.20964/2016.08.38
3. Lee, S. G., Lee, S., & Lee, H. I. (2001). Photocatalytic production of hydrogen from aqueous solution containing CN^- as a hole scavenger. *Appl. Catal. A*, 207, 173–181. DOI: 10.1016/S0926-860X(00)00671-2
4. Ando, M., Zehetner, J., Kobayashi, T., & Haruta, M. (1996). Large optical CO sensitivity of NO^2-pretreated Au-NiO composite films. *Sens. Actuators B*, *36*, 513–516. DOI: 10.1016/S0925-4005(97)80121-9
5. Múčka, V., & Baburek, E. (1998). Catalytic properties of nickel-yttrium mixed oxides and the influence of ionizing radiation. *Rad. Phys. Chem.*, *53*, 483–489. DOI: 10.1016/S0969-806X(98)00216-3
6. Lee, C. B., B. S. Kang, B. S., Benayad, A., Lee, M. J., Ahn, S.-E., Kim, K. H., … & Yoo, I. K. (2008). Effects of metal electrodes on the resistive memory switching property of NiO thin films. *Appl. Phys. Lett.*, *93*, 042115. DOI: 10.1063/1.2967194
7. Tsymbal, E. Y., & Pettifor, D. G. (2001). Perspectives of giant magnetoresistance. *Solid State Phys.*, *56*, 113–237. DOI: 10.1016/S0081-1947(01)80019-9
8. Roth, W. L. (1958). Magnetic structures of MnO, FeO, CoO, and NiO. P*hys. Rev.*, *110*, 1333–1341. DOI: 10.1103/PhysRev.110.1333

9. Hutchings, M. T., & Samuelsen, E. J. (1972). Measurement of spin-wave dispersion in NiO by inelastic neutron scattering and its relation to magnetic properties. *Phys. Rev. B*, *6*, 3447–3461. DOI: 10.1103/PhysRevB.6.3447
10. Hillebrecht, F. U., Ohldag, H., Weber, N. B., Bethke, C., Mick, U., Weiss, M., & Bahrdt, J. (2001). Magnetic moments at the surface of antiferromagnetic NiO(100). *Phys. Rev. Lett*., *86*, 3419–3422. DOI: 10.1103/PhysRevLett.86.3419
11. Rooksby, H. P. (1948). A note on the structure of nickel oxide at subnormal and elevated temperatures. *Acta Crystallogr*., *1*, 226. DOI: 10.1107/S0365110X48000612
12. Slack, G. A. (1960). Crystallography and domain walls in antiferromagnetic NiO crystals, *J. Appl. Phys*., *31*, 1571–1582. DOI: 10.1063/1.1735895
13. Massarotti, V., Capsoni, D., Berbenni, V., Riccardi, R., Marini, A., & Antolini, E. (1991). Structural characterization of nickel oxide. *Z. Naturforsch. A*, *46*, 503–512. DOI: 10.1515/zna-1991-0606
14. Rodic, D., Spasojevic, V., Kusigerski, V., Tellgren, R., & Rundlof, H. (2000). Magnetic ordering in polycrystalline $Ni_xZn_{1-x}O$ solid solutions. *Phys. Status Solidi B*, *218*, 527–536. DOI: 10.1002/1521-3951(200004)218:2<527::AID-PSSB527>3.0.CO;2- I
15. Balagurov, A. M., Bobrikov, I. A., Sumnikov, S. V., Yushankhai, V. Y., & Mironova-Ulmane, N. (2016). Magnetostructural phase transitions in NiO and MnO: neutron diffraction data. *JETP Lett.*, *104*, 88–93. DOI: 10.1134/S0021364016140071
16. Chung, E. M. L., Paul, D. M., Balakrishnan, G., Lees, M. R., Ivanov, A., & Yethiraj, M. (2003). Role of electronic correlations on the phonon modes of MnO and NiO. *Phys. Rev. B*, *68*, 140406. DOI: 10.1103/PhysRevB.68.140406
17. Luo, W., Zhang, P., & Cohen, M. L. (2007). Splitting of the zone-center phonon in MnO and NiO. *Solid State Commun*., *142*, 504–508. DOI: 10.1016/j.ssc.2007.03.047
18. Kant, C., Mayr, F., Rudolf, T., Schmidt, M., Schrettle, F., Deisenhofer, J., & Loidl, A. (2009). Spin-phonon coupling in highly correlated transition-metal monoxides. *Eur. Phys. J. Special Topics*, *180*, 43–59. DOI: 10.1140/epjst/e2010-01211-6
19. Mørup, S., Madsen, D. E., Frandsen, C., Bahl, C. R. H., & Hansen, M. F. (2007). Experimental and theoretical studies of nanoparticles of antiferromagnetic materials. *J. Phys.: Condens. Matter*, *19*, 213202. DOI: 10.1088/0953-8984/19/21/213202
20. Nakahigashi, K., Fukuoka, N., & Shimomura, Y. (1975). Crystal structure of antiferromagnetic NiO determined by X-ray topography. *J. Phys. Soc. Jpn*., *38*, 1634–1640. DOI: 10.1143/JPSJ.38.1634
21. Kodama, R. H., Makhlouf, S. A., & Berkowitz, A. E. (1997). Finite size effects in antiferromagnetic NiO nanoparticles. *Phys. Rev. Lett*., *79*, 1393–1396. DOI: 10.1103/PhysRevLett.79.139
22. Kodama, R. H., & Berkowitz, A. E. (1999). Atomic-scale magnetic modelling of oxide nanoparticles. *Phys. Rev. B*, *59*, 6321–6336. DOI: 10.1103/PhysRevB.59.6321.
23. Tiwari, S. D., & Rajeev, K. P. (2006). Magnetic properties of NiO nanoparticles, *Thin Solid Films*, *505*, 113–117. DOI: 10.1016/j.tsf.2005.10.019
24. Mandal, S., Banerjee, S., & Menon, K. S. R. (2009). Core-shell model of the vacancy concentration and magnetic behavior for antiferromagnetic nanoparticle. *Phys. Rev. B*, *80*, 214420. DOI: 10.1103/PhysRevB.80.214420
25. Mandal, S., Menon, K. S. R., Mahatha, S. K., & Banerjee, S. (2011). Finite size versus surface effects on magnetic properties of antiferromagnetic particles. *Appl. Phys. Lett.*, *99*, 232507. DOI: 10.1063/1.3668091
26. Cooper, J. F. K., Ionescu, A., Langford, R. M., Ziebeck, K. R. A., Barnes, C. H. W., Gruar, R., … & Ouladdiaf, B. (2013). Core/shell magnetism in NiO nanoparticles. *J. Appl. Phys*., *114*, 083906. DOI: 10.1063/1.4819807

27. Balagurov, A. M., Bobrikov, I. A., Grabis, J., Jakovlevs, D., Kuzmin, A., Maiorov, M., & Mironova-Ulmane, N. (2013). Neutron scattering study of structural and magnetic size effects in NiO. *IOP Conf. Ser.: Mater. Sci. Eng.*, *49*, 012021. DOI: 10.1088/1757-899X/49/1/012021
28. Yang, Z., Gao, D., Tao, K., Zhang, J., Shi, Z., Xu, Q., Shi, S., & Xue, D. (2014). A series of unexpected ferromagnetic behaviors based on the surface-vacancy state: an insight into NiO nanoparticles with a core-shell structure. *RSC Adv*., *4*, 46133–46140. DOI: 10.1039/C4RA06472K
29. Balagurov, A. M., Bobrikov, I. A., Sumnikov, S. V., Yushankhai, V. Y., Grabis, J., Kuzmin, A., … & Sildos, I. (2016). Neutron diffraction study of microstructural and magnetic effects in fine particle NiO powders. *Phys. Status Solidi B*, *253*, 1529–1536. DOI: 10.1002/pssb.201552680
30. Richardson, J. T., Yiagas, D. I., Turk, B., Forster, K., & Twigg, M. V. (1991). Origin of superparamagnetism in nickel oxide. *J. Appl. Phys*., *70*, 6977–6982. DOI: 10.1063/1.349826
31. Klausen, S. N., Lindgärd, P. A., Lefmann, K., Bødker, F., & Mørup, S. (2002). Temperature dependence of the magnetization of disc shaped NiO nanoparticles. *Phys. Status Solidi A*, *189*, 1039–1042. DOI: 10.1002/1521- 396X(200202)189:3<1039::AID-PSSA1039>3.0.CO;2-A
32. Li, L., Chen, L., Qihe, R., & Li, G. (2006). Magnetic crossover of NiO nanocrystals at room temperature. *Appl. Phys. Lett*., *89*, 134102. DOI: 10.1063/1.2357562
33. Makhlouf, S. A., Kassem, M. A., & Abdel-Rahim, M. A. (2009). Particle size-dependent electrical properties of nanocrystalline NiO. *J. Mater. Sci.*, *44*, 3438–3444. DOI: 10.1007/s10853-009-3457-0
34. Duan, W. J., Lu, S. H., Wu, Z. L., & Wang, Y. S. (2012). Size effects on properties of NiO nanoparticles grown in alkalisalts. *J. Phys. Chem. C*, *116*, 26043–26051. DOI: 10.1021/jp308073c
35. Dietz, R. E., Parisot, G. I., & Meixner, A. E. (1971). Infrared absorption and Raman scattering by two-magnon processes in NiO. *Phys. Rev. B*, *4*, 2302–2310. DOI: 10.1103/PhysRevB.4.2302
36. Dietz, R. E., Brinkman, W. F., Meixner, A. E., & Guggenheim, H. J. (1971). Raman scattering by four magnons in NiO and $KNiF_3$. *Phys. Rev. Lett*., *27*, 814–817. DOI: 10.1103/PhysRevLett.27.814
37. Lockwood, D. J., Cottam, M. G., & Baskey, J. H. (1992). One- and two-magnon excitations in NiO. *J. Magn. Magn. Mater*., *104*, 1053–1054. DOI: 10.1016/0304-8853(92)90486-8
38. Pressl, M., Mayer, M., Knoll, P., Lo, S., Hohenester, U., & Holzinger-Schweiger, E. (1996). Magnetic Raman scattering in undoped and doped antiferromagnets. *J. Raman Spectroscopy*, *27*, 343–349. DOI: 10.1002/(SICI)1097-4555(199603)27:3/4<343::AID-JRS956>3.0.CO;2-S
39. Grimsditch, M., McNeil, L. E., & Lockwood, D. J. (1998). Unexpected behavior of the antiferromagnetic mode of NiO. *Phys. Rev. B*, *58*, 14462–14466. DOI: 10.1103/PhysRevB.58.14462
40. Cazzanelli, E., Kuzmin, A., Mariotto, G., & Mironova-Ulmane, N. (2003). Study of vibrational and magnetic excitations in $Ni_cMg_{1-c}O$ solid solutions by Raman spectroscopy. *J. Phys.: Condensed Matter*, *15*, 2045. DOI: 10.1088/0953-8984/15/12/321
41. Cazzanelli, E., Kuzmin, A., Mironova-Ulmane, N., & Mariotto, G. (2005). Behavior of one-magnon frequency in antiferromagnetic $Ni_cMg_{1-c}O$ solid solutions. *Phys. Rev. B*, *71*, 134415. DOI: 10.1103/PhysRevB.71.134415

42. Aytan, E., Debnath, B., Kargar, F., Barlas, Y., Lacerda, M. M., Li, J. X., … & Balandin, A. A. (2017). Spin-phonon coupling in antiferromagnetic nickel oxide. *Appl. Phys. Lett*., *111*, 252402. DOI: 10.1063/1.5009598
43. Haywood, B. C. G., & Collins, M. F. (1969). Lattice dynamics of MnO. *J. Phys. C: Solid State Phys*., *2*, 46. DOI: 10.1088/0022-3719/2/1/306
44. Haywood, B. C. G., & Collins, M. F. (1971). Optical phonons in MnO. *J. Phys. C: Solid State Phys*., *4*, 1299. DOI: 10.1088/0022-3719/4/11/005
45. Upadhyaya, K. S., & Singh, R. K. (1974). Shell model lattice dynamics of transition metal oxides. *J. Phys. Chem. Solids*, *35*, 1175–1179. DOI: 10.1016/S0022- 3697(74)80137-X
46. Reichardt, W., Wagner, V., & Kress, W. (1975). Lattice dynamics of NiO. *J. Phys. C: Solid State Phys.*, *8*, 3955. DOI: 10.1088/0022-3719/8/23/009
47. Coy, R. A., Tompson, C. W., & Gürmen, E. (1976). Phonon dispersion in NiO. *Solid State Commun.*, *18*, 845–847. DOI: 10.1016/0038-1098(76)90220-9
48. Savrasov, S. Y., & Kotliar, G. (2003). Linear response calculations of lattice dynamics in strongly correlated systems. *Phys. Rev. Lett*., *90*, 056401. DOI: 10.1103/PhysRevLett.90.056401
49. Massidda, S., Posternak, M., Baldereschi, A., & Resta, R. (1999). Noncubic behavior of antiferromagnetic transition-metal monoxides with the rocksalt structure. *Phys. Rev. Lett.*, *82*, 430–433. DOI: 10.1103/PhysRevLett.82.430
50. Mironova-Ulmane, N., Kuzmin, A., Steins, I., Grabis, J., Sildos, I., & Pärs, M. (2007). Raman scattering in nanosized nickel oxide NiO. *J. Phys.: Conf. Ser.*, *93*, 012039. DOI: 10.1088/1742-6596/93/1/012039
51. Mironova-Ulmane, N., Kuzmin, A., Grabis, J., Sildos, I., Voronin, V., Berger, I., & Kazantsev, V. (2011). Structural and magnetic properties of nickel oxide nanopowders. *Solid State Phenomena*, *168–169*, 341–344. DOI: 10.4028/www.scientific.net/SSP.168-169.341
52. Gandhi, A. C., Pant, J., Pandit, S. D., Dalimbkar, S. K., Chan, T.-S., Cheng, C.-L., … & Wu, S. Y. (2013). Short-range magnon excitation in NiO nanoparticles. *J. Phys. Chem. C*, *117*, 18666–18674. DOI: 10.1021/jp4029479
53. Ravikumar, P., Kisan, B., & Perumal, A. (2015). Enhanced room temperature ferromagnetism in antiferromagnetic NiO nanoparticles. *AIP Adv*., *5*, 087116. DOI: 10.1063/1.4928426
54. Mironova-Ulmane, N., Kuzmin, A., & Sildos, I. (2015). Template-based synthesis of nickel oxide. *IOP Conf. Ser.: Mater. Sci. Eng.*, *77*, 012025. DOI: 10.1088/1757-899X/77/1/012025
55. Mironova-Ulmane, N., Kuzmin, A., Sildos, I., & Pärs, M. (2011). Polarisation dependent Raman study of single-crystal nickel oxide. *Centr. Eur. J. Phys*., *9*, 1096–1099. DOI: 10.2478/s11534-010-0130-9
56. Mironova-Ulmane, N., Kuzmin, A., Skvortsova, V., & Sildos, I. (2002). Exciton-magnon interactions in $Ni_cMg_{1-c}O$ single-crystals. *Phys. Solid State*, *44*, 1463–1467. DOI: 10.1134/1.1501338
57. Ishikawa, K., Fujima, N., & Komura, H. (1985). First-order Raman scattering in MgO micro-crystals. *J. Appl. Phys*., *57*, 973–975. DOI: 10.1063/1.334701
58. Gouadec, G., & Colomban, P. (2007). Raman Spectroscopy of nanomaterials: How spectra relate to disorder, particle size and mechanical properties. *Progr. Crystal Growth Charact. Mater*., *53*, 1–56. DOI: 10.1016/j.pcrysgrow.2007.01.001
59. Alders, D., Tjeng, L. H., Voogt, F. C., Hibma, T., Sawatzky, G. A., Chen, C. T., & Iacobucci, S. (1998). Temperature and thickness dependence of magnetic moments in NiO epitaxial films. *Phys. Rev. B*, *57*, 11623–11631. DOI: 10.1103/PhysRevB.57.11623

MAGNONU UN FONONU IEROSINĀŠANAS NANOIZMĒRA NiO

A N. Mironova-Ulmane, A. Kuzmins,
I. Sildos, L. Puust, J. Grabis

K o p s a v i l k u m s

Monokristāliskais, mikrokristāliskais un nanokristāliskais niķeļa oksīdi (NiO) tika pētīti, izmantojot Ramana spektroskopiju. Monokristāliskos NiO(100), NiO(110) un NiO(111) ir novērota jauna josla ap 200 cm^{-1} un TO-LO joslas sadalīšanās ap 350-650 cm^{-1}. Mikrokristāliska (1500 nm) un nanokristāliska (13-100 nm) NiO Ramana spektri ir līdzīgi monokristāliskam oksīdam. Tie visi satur divu magnonu joslu ap 1500 cm^{-1}, kas norāda, ka pie istabas temperatūras nanooksīdi atrodas antiferomagnētiskā stāvoklī. Nanokristāliskos NiO ir novērota arī jauna asa josla ap 500 cm^{-1}, kuras temperatūras atkarība norāda uz tās magnētisko izcelsmi, iespējams, saistītu ar fonona-magnonu ierosmi Briljuena zonas centrā.

23.11.2018.